Anisotropic Graphene

by

Brett Meggison

A thesis submitted to the Faculty of Graduate Studies of
THE UNIVERSITY OF MANITOBA
in partial fulfilment of the requirements of the degree of

MASTER OF SCIENCE

Department of Physics and Astronomy
University of Manitoba
Winnipeg

THE UNIVERSITY OF MANITOBA

Abstract

Faculty of Science
Department of Physics and Astronomy

Master of Science

by Brett Meggison

The generation of a gap in graphene has potentially useful implications for the production of electrical components. Experimentally the gapped (insulating) state has never been observed. Theorists would like to provide information on how a gap could be produced. We study the effect on the critical coupling of straining a graphene lattice. We work with a low energy effective theory obtained by considering a tight-binding Hamiltonian expanded around the Dirac points in momentum space.

Acknowledgements

I would like to thank my supervisors Andrew Frey and Margaret Carrington for their guidance and patience during the course of my classes, research, and thesis writing process. I think it is a rare thing to find people so dedicated to their craft while being as kind as they are to people wishing to follow in their footsteps. I would like to thank my family for their support in my endeavours, and I know I would not have been able to finish this without their encouragement. I would like thank the excellent teachers I have had the pleasure to learn from, from my high-school science teachers, who first instilled an excitement for science in me, to the dedicated faculty at Brandon University who first encouraged me to continue my studies by entering graduate school, to the professors at the universities of Manitoba and Winnipeg who patiently shared their knowledge with me. I am a lucky individual to be surrounded by these people, and I hope I can do their efforts justice by producing honest, quality work of my own.

Contents

List of Figures

Chapter 1

Introduction

From the point of view of quantum field theorists, graphene is interesting because it has similar features to quantum chromodynamics (QCD). Graphene is described by three-dimensional quantum electrodynamics (QED), which is strongly coupled. In this sense, it behaves more like QCD than like conventional four-dimensional QED. However, QCD is a non-abelian gauge theory, while QED is abelian. These two points combined mean that graphene is a good toy model for methods applicable to QCD calculations (such as Schwinger-Dyson equations), because it shares some aspects (strong coupling) but is significantly simpler in others (the gauge transformations are commutative).

At the most practical level, people are interested in graphene for is potential application in a wide range of electronic products/components, including batteries, transistors, inductors, and entire circuits and screens made of the durable and flexible material [8, 9, 17]. There are a few characteristics that make graphene such an appealing material for electronics. The first is the fact that it is a ballistic conductor, which means the ratio of mean free path length of the charge carriers [12] (i.e. how far the electrons move before scattering off of another electron) to the length of the channel (the length a charge carrier is expected to travel before hitting the "walls" of the conductor) is greater than or equal to one. The graphene lattice is also strong and flexible, thanks to the trigonal, filled σ bonds between atoms [11]. Graphene exists naturally in what is called a semi-metal

state [7]. This state is conducting (as there is no band-gap), but does not behave like a traditional conductor because the electron density of states goes to zero at the energies where the bands meet. The semi-metal state has exciting uses for the material, as just how much current is carried by it can be altered to best fit the situation. For example, this would be useful in the creation of graphene field-effect transistors, which currently have a very high leaking current when in the off state [14]. Inducing an insulator state into graphene would make these transistors more efficient at blocking current when in the this off state. The critical coupling is the variable we use to mark the phase-change from insulating to semi-metal state. Currently, most calculations place the critical coupling at around $\alpha_c \approx 2.8 - 3.2$, but the maximum coupling that can be obtained is $\alpha_{max} \approx 2.2$ [1]. Various ideas have been proposed to reduce the critical coupling and create a gap. In this thesis we look at one proposal, which is to strain the graphene sheet.

Near the Dirac points of the graphene lattice, the density of states goes to zero, which leaves the electrons almost totally unscreened from the coulomb interaction. However, it is widely accepted that this interaction is not strong enough to generate a gap by itself. It has been suggested that deforming the Dirac cone will be enough to cause gap generation by breaking the chiral symmetry of the system [3].

Chapter 2 covers how we obtain the dressing functions which we renormalized. In section 2.1 we begin by reviewing the derivation of the isotropic theory. We cover the free fermion part of the Lagrangian in subsection 2.1.1. The free photon and interacting parts of the Lagrangian are covered in subsection 2.1.2. We list the bare Feynman rules that can be obtained from the Lagrangian given in the previous two subsections in subsection 2.1.3. Subsection 2.1.4 explains why graphene is a strongly coupled, and therefore non-perturbative, system. In section 2.3 we show how the theory can be modified to arrive at an anisotropic model. We define an anisotropy parameter (η) that characterizes the degree of anisotropy, relative to the original isotropic case which corresponds to $\eta = 1$ This thesis is organized as follows. In Chapter 3 we review various approximations that have been used in previous work. We discuss the importance and justification of

these approximations, and explain which of them we have used and why. Some level of approximations is a necessity because of the numerical difficulties involved in solving non-perturbative integral equations. The work presented in this thesis relaxes many assumptions that are widely known or suspected to be not well justified, but are commonly adopted for numerical practicallity. In Chapter 4 we give some details of our numerical method. We discuss our interpolation and integration techniques, and some of the coding techniques/software libraries used to acheive acceptable computational speed. We present and make notes on our results in Chapter 5, and draw our conclusions in Chapter 6

Throughout the thesis we will use capital letters (P, K, Q) for three momenta, which are defined, for example, $P = (p_0, \vec{p})$ with $\vec{p} = (p^1, p^2)$. We will frequently use the notation $p_1 = p_x$ and $p_2 = p_y$ and we will write $p = \sqrt{p_x^2 + p_y^2}$. Greek indices μ, ν, etc. run from 0, 1, 2. The notation is slightly different in section 2.1.2 where we derive the action for the dimensionally reduced version of QED that we will use. When describing bare propagators, a superscript (0) is used, e.g. $S^{(0)}(K)$ is the bare fermion propagator. Throughout, notation for the inverse, e.g. S^{-1}, is in reference to the matrix inverse, not the multiplicative inverse.

Chapter 2

Theory

2.1 Isotropic Graphene

2.1.1 Fermions

Graphene is composed of carbon atoms arranged in a hexagonal lattice. A six-point (hexagonal) lattice can be decomposed into two three-point (triangular) lattices (which we will refer to as A and B), with the decomposition being chosen so that lattice points

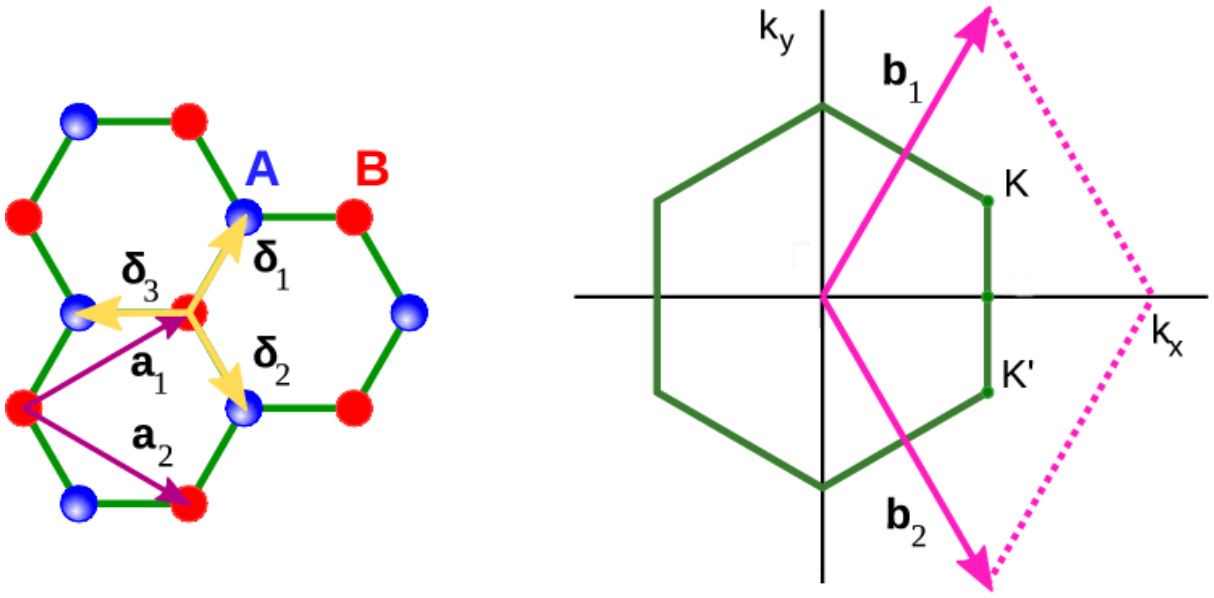

FIGURE 2.1: Left: Notation for hexagonal graphene unit cell. Right: Brillouin zone

(a and b) alternate between belonging to the A and B lattices respectively when moving between closest neighbours. Figure 2.1 shows the hexagonal lattice and corresponding Brillouin zone. $\vec{n}$ is the vector which describes the location of a lattice point on A, and can be given as a linear combination of the vectors a_1 and a_2, which are defined as

$$a_1 = \frac{a}{2}(3, \sqrt{3}), \quad a_2 = \frac{a}{2}(3, -\sqrt{3}). \tag{2.1}$$

We use $\vec{\delta}$ for the nearest neighbour vectors that connects adjacent sites on the A and B lattices. We can define the displacement vectors as follows.

$$\delta_1 = \frac{a}{2}(1, \sqrt{3}), \quad \delta_2 = \frac{a}{2}(1, -\sqrt{3}), \quad \delta_3 = -a(1, 0) \tag{2.2}$$

We can describe the nearest-neighbour motion of the electrons on these lattices using an appropriate set of four creation/annihilation operators. That is, an electron "hops" from point a to b by being annihilated at a (corresponding operator $a_{\vec{n},\sigma}$) and created at b (corresponding operator $b^{\dagger}_{\vec{n}+\vec{\delta},\sigma}$), where σ is the spin. The sum of all the hops gives us a tight binding Hamiltonian (see [5])

$$H = -t \sum_{\vec{n},\vec{\delta},\sigma} \left[a^{\dagger}_{\vec{n},\sigma} b_{\vec{n}+\vec{\delta},\sigma} + a_{\vec{n},\sigma} b^{\dagger}_{\vec{n}+\vec{\delta},\sigma} \right], \tag{2.3}$$

where t is the nearest neighbour hopping parameter, representing the energy involved in each hop. We want to show how to use this Hamiltonian to get a low energy effective theory. First we want to transition into momentum space and take advantage of the periodic characteristics of our system. To illustrate the method, we start with a 1-D function $f(n)$ defined on some discrete set of points analogous to sites on a 1-D lattice. We can relate it to a function of a continuous variable x

$$f(x) = \sqrt{L} \sum_{n=-\infty}^{\infty} f(n)\delta(x - nL), \tag{2.4}$$

where L is the length between the points $f(n)$ is defined on, and the factor of $\sqrt{L}$ is a

convention to fix the dimension. The Fourier transform of $f(x)$ and the inverse transform are

$$\begin{aligned} \tilde{f}(k) =& \sqrt{L}\sum_n e^{-iknL} f(n) \\ f(x) =& \int_{-\infty}^{\infty} \frac{dk}{2\pi} e^{ikx} \tilde{f}(k). \end{aligned} \tag{2.5}$$

Equation (2.5) is a discrete Fourier transform with k having a period of Q, and the Fourier constants given by

$$\begin{aligned} \sqrt{L} f(n) &= \frac{1}{Q}\int_0^Q dk \tilde{f}(k) e^{i2\pi nk/Q} \\ \implies f(n) &= \frac{\sqrt{L}}{2\pi}\int_0^Q dk \tilde{f}(k) e^{inkL} \end{aligned} \tag{2.6}$$

where $Q = \frac{2\pi}{L}$. To extend to 2-D, we take $nL \to \vec{n} = \sum_{i=1}^{2} n_i \vec{a}_i$, where $\vec{a}_i$ are the lattice vectors. We also take $nLk \to \vec{n}\cdot\vec{k}$ and the 1-D momentum integral over $(0, Q)$ becomes a 2-D integral over the Brillouin zone, shown in the right panel of figure 2.1. The reciprocal lattice vectors shown in the figure are given by

$$b_1 = \frac{2\pi}{3a}(1, \sqrt{3}), \quad b_2 = \frac{2\pi}{3a}(1, -\sqrt{3}). \tag{2.7}$$

Due to the periodicity of the hexagonal lattice, the Brillouin zone is sufficient for considering the electron's behaviour as can be seen in equations (2.6). Any point in the momentum phase space is reached by taking $k \to k + nb_1 + mb_2$ where k is in the Brillouin zone and $m, n \in \mathbb{Z}$.

Our general function $f(n)$ defined on a set of lattice points was the 1-D analogy to the creation/annihilation operators for the fermions in our tight-binding model. In analogy with equation (2.6), we can write our creation and annihilation operators, which are defined on the two dimensional lattice sites, as integrals over a functions of a continuous variable defined on the Brillouin zone. For example,

$$a_{\vec{n},\sigma} = \sqrt{S}\int_{BZ} \frac{d^2k}{(2\pi)^2} e^{i\vec{k}\cdot\vec{n}} a_\sigma(\vec{k}), \tag{2.8}$$

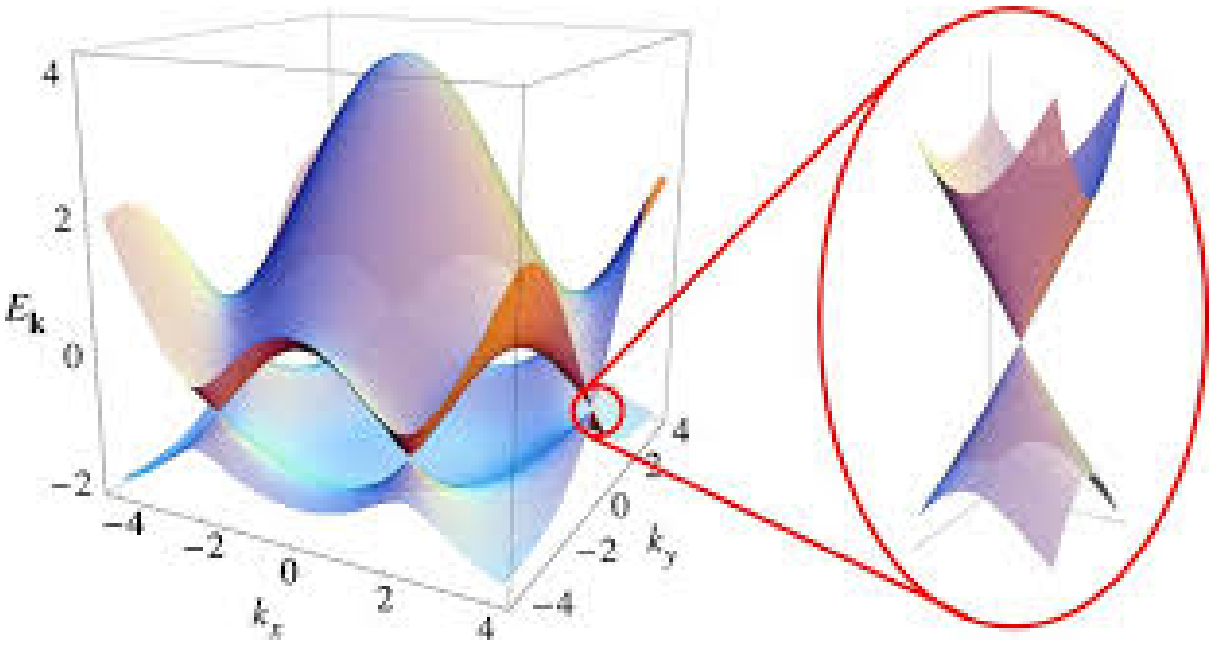

FIGURE 2.2: Conduction and Valence Bands

and similarly for b, $a^\dagger$, and $b^\dagger$. Substituting these expressions into equation (2.3) we arrive at

$$H = -t \sum_{\sigma} \sum_{\vec{\delta}} \int_{BZ} \frac{d^2k}{(2\pi)^2} \left[a_\sigma^\dagger(\vec{k}) b_\sigma(\vec{k}) e^{-i\vec{\delta}\cdot\vec{k}} + a_\sigma(\vec{k}) b_\sigma^\dagger(\vec{k}) e^{i\vec{\delta}\cdot\vec{k}} \right]. \tag{2.9}$$

In order to obtain the equation for the energy bands, we rewrite (2.9) as

$$H = -t \sum_{\sigma} \sum_{\delta} \int_{BZ} \frac{d^2k}{(2\pi)^2} \begin{bmatrix} a_\sigma^\dagger(\vec{k}) & b_\sigma^\dagger(\vec{k}) \end{bmatrix} \begin{bmatrix} 0 & e^{-i\vec{\delta}\cdot\vec{k}} \\ e^{i\vec{\delta}\cdot\vec{k}} & 0 \end{bmatrix} \begin{bmatrix} a_\sigma(\vec{k}) \\ b_\sigma(\vec{k}) \end{bmatrix}. \tag{2.10}$$

We can obtain the eigenenergies by diagonalizing the matrix in equation (2.10) to yield

$$\begin{aligned} E(k) &= \pm \left| t \sum_{\vec{\delta}} e^{-i\vec{\delta}\cdot\vec{k}} \right| \\ &= \pm t \sqrt{\sum_j e^{-i\vec{\delta}_j\cdot\vec{k}} \sum_h e^{i\vec{\delta}_h\cdot\vec{k}}}. \end{aligned} \tag{2.11}$$

The $+$ sign represents the conductive band, and the $-$ sign gives the valence band. Rearranging (2.11) gives

$$E(k) = \pm t\sqrt{3 + f(k)} \tag{2.12}$$

$$f(k) = 2\cos\left(\sqrt{3}k_y a\right) + 4\cos\left(\frac{\sqrt{3}}{2}k_y a\right)\cos\left(\frac{3}{2}k_x a\right). \tag{2.13}$$

Of particular interest are the six Dirac points at the corners of the Brillouin zone. These points minimize the energy dispersion relation, as can be seen in figure 2.2. We choose two inequivalent Dirac points, the K-points, which are given by

$$K = \left(\tfrac{2\pi}{3a}, \tfrac{2\pi}{3\sqrt{3}a}\right) \tag{2.14}$$

$$K' = \left(\tfrac{2\pi}{3a}, -\tfrac{2\pi}{3\sqrt{3}a}\right). \tag{2.15}$$

Two more Dirac points are given by the negative of equations (2.14) and (2.15), and the final two are given by $\pm K \mp K' = (0, \pm\frac{4\pi}{3\sqrt{3}a})$.

Next we discuss how to obtain an effective action that describes the theory at low energies. As can be seen from figure 2.2, near the Dirac points, the dispersion relation is conical. When we expand equations (2.12) and (2.13) around the point $k = K + p,\ |p| \ll |K|$ the dispersion relation becomes

$$E(p) = v_F|p| + \mathcal{O}\left(\left(\frac{p}{K}\right)^2\right) \tag{2.16}$$

where we have defined $v_F = 3at/2$.

Another way to obtain this result is to rewrite the Hamiltonian by defining a spinor

$$\Psi_\sigma(\vec{p}) = \left(a_\sigma(\vec{K}_+ + \vec{p}), b_\sigma(\vec{K}_+ + \vec{p}), b_\sigma(\vec{K}_- + \vec{p}), a_\sigma(\vec{K}_- + \vec{p})\right). \tag{2.17}$$

Expanding in $|p| \ll |K|$ and taking the leading order term we find

$$H_0 = \frac{3at}{2}\sum_\sigma \int \frac{d^2p}{(2\pi)^2}\bar{\Psi}_\sigma(\vec{p})\left(\gamma^1 p_1 + \gamma^2 p_2\right)\Psi_\sigma(\vec{p}). \tag{2.18}$$

From this Hamiltonian we can obtain the Lagrangian.

At this point, we will perform a Wick rotation, and from now on all equations will be expressed in Euclidean space. The Lagrangian takes the form

$$\mathcal{L} = \sum_{\sigma} \bar{\Psi}_{\sigma}(t, \vec{x}) \left[i M^{\mu\nu} \gamma_{\nu} \right] \partial_{\mu} \Psi_{\sigma}(t, \vec{x}) \tag{2.19}$$

where we have defined M

$$M = \begin{bmatrix} 1 & 0 & 0 \\ 0 & v_{Fx} & 0 \\ 0 & 0 & v_{Fy} \end{bmatrix} \tag{2.20}$$

with $v_{Fx} = v_{Fy} = v_F = \frac{3at}{2}$. It is interesting to note the similarity between (2.19) and the Dirac Lagrangian for relativistic, massless fermions. The K points in the Brillouin zone are called Dirac-points because expansion around them yields this familiar Lagrangian, and this is why we say fermions close to the Dirac points behave as massless Dirac fermions.

2.1.2 Photons

Next we need to include the kinetic photon term in the Lagrangian. Unlike the fermions, the photons are not constrained to the graphene plane, but can propagate perpendicular to the plane. To combine the behaviour of photons with the fermions living on the graphene sheet, we dimensionally reduce the usual (1+3)-D Maxwell action and obtain the brane action, [4, 10]. We will work in the Landau gauge, which is the Lorenz gauge $\mathcal{L}_{\text{gf}} = -\frac{(\partial_{\mu} A^{\mu})^2}{2\xi}$ with $\xi \to 0$.

We start with the full 4-D effective action (which is abelian and is invariant under local gauge transformations), ignoring the purely kinetic term for a free fermion:

$$S = \int d^4x \left(\frac{1}{4} F_{\mu\nu} F^{\mu\nu} + ie\overline{\psi} \not{A} \psi \right) - \frac{\left(\partial_{\mu} A^{\mu}\right)^2}{2\xi}. \tag{2.21}$$

We trace and integrate out the 4-D gauge field A^μ to yield

$$S = \frac{1}{2}\int d^4x d^4y J^\mu(x)\hat{G}^0_{\mu\nu}(x-y)J^\nu(y) \tag{2.22}$$

with $J^\mu = e\overline{\psi}\gamma^\mu\psi$ and $\hat{G}^0$ is the bare propagator. Since we are considering a case where the fermion movement is restricted to the lattice plane, we can set the component of the fermion current which is perpendicular to the lattice plane to zero: $J^3 = 0$. We can then define the other fermion currents as $J^\mu = j^\mu\delta(x_3)$ where $\mu \in \{0,1,2\}$. After performing a Fourier transform and defining $\mathcal{D}^4k = \frac{d^4k}{(2\pi)^4}$, the bare propagator is given by

$$\hat{G}^0_{\mu\nu}(x-y) = \int \mathcal{D}^4k\, e^{ik(x-y)}\left(\delta_{\mu\nu} - (1-\xi)\frac{k_\mu k_\nu}{k^2}\right)\frac{1}{k^2} \tag{2.23}$$

where $k = \sqrt{k_0^2+k_1^2+k_2^2+k_3^2} = \sqrt{K^2+k_3^2}$ is the magnitude of the 4-D momentum vector.

The bare propagator now becomes

$$\hat{G}^0_{\mu\nu}(x-y) = \int \mathcal{D}^4k\, e^{ik(x-y)}\left(\delta_{\mu\nu} - (1-\xi)\frac{k_\mu k_\nu}{K^2+k_3^2}\right)\frac{1}{K^2+k_3^2}. \tag{2.24}$$

Integrating with respect to k_3 yields

$$G^0_{\mu\nu}(X-Y) = \frac{1}{2}\int \mathcal{D}^3K e^{iK(X-Y)}\left(\delta_{\mu\nu} - (1-\xi)\frac{K_\mu K_\nu}{K^2}\right)\frac{1}{\sqrt{K^2}}. \tag{2.25}$$

Compare equations (2.23) and (2.25). Other than the reduced dimension, if we take $k \to K$ they differ by a factor of $\frac{\sqrt{K^2}}{2}$. The effective action is therefore defined

$$S_{\text{eff}} = \int d^3x \left(\frac{1}{2}F_{\mu\nu}\frac{1}{\sqrt{-\partial^2}}F^{\mu\nu} + A_\mu j^\mu + \frac{1}{\xi}\partial_\mu A^\mu \frac{1}{\sqrt{-\partial^2}}\partial_\nu A^\nu\right) \tag{2.26}$$

where A_μ and its field strength tensor are 3-D. The propagator obtained from this action is the dimensionally reduced propagator in (2.25). In the next section we will combine this result with the contribution to the action from the free fermion Lagrangian in Eq. (2.19).

2.1.3 Feynman Rules

Combining equations (2.19) with (2.26) we get our action

$$S = \int d^3x \sum_a \left(\bar{\psi}_a \left(i\partial_\mu - eA_\mu\right) M^{\mu\nu}\gamma_\nu\psi_a\right) + F_{\mu\nu}\frac{1}{2\sqrt{-\partial^2}}F^{\mu\nu} + \text{gauge fixing.} \tag{2.27}$$

We can construct the generating function from the action and then use functional derivatives to obtain the bare propagators. Note we also perform a Fourier transform to put the propagators in momentum space. We give the Feynman Rules below (see Appendices A, B, and subsection 2.1.2 for further details).

- $F_{\mu\nu}\frac{1}{2\sqrt{-\partial^2}}F^{\mu\nu}$ + gauge fixing gives the bare photon propagator, as was seen in equation (2.25).
$$G^{(0)}_{\mu\nu} = \left(\frac{\delta^2\mathcal{L}}{\delta A^\mu \delta A^\nu}\Big|_{A_\mu=0}\right)^{-1} = \left[\delta_{\mu\nu} - \frac{P_\mu P_\nu}{P^2}\right]\frac{1}{2\sqrt{P^2}}$$
- $\overline{\psi}_a i\partial_\mu M^{\mu\nu}\gamma_\nu\psi_a$ gives the bare fermion propagator.
$$S^{(0)}(P) = \left(\frac{\delta^2\mathcal{L}}{\delta\overline{\psi}\delta\psi}\Big|_{\overline{\psi}=\psi=0}\right)^{-1} = -\left[i\gamma^\mu M_{\mu\nu}P^\nu\right]^{-1}$$
- $\overline{\psi}_a eA_\mu M^{\mu\nu}\gamma_\nu\psi_a$ gives the bare vertex
$$\Gamma^{(0)}_\mu = \left(\frac{\delta^3\mathcal{L}}{\delta A^\mu\delta\overline{\psi}\delta\psi}\Big|_{A^\mu=\overline{\psi}=\psi=0}\right)^{-1} = eM_{\mu\nu}\gamma^\nu\,. \tag{2.28}$$

2.1.4 Strong Coupling

To understand why graphene is a strongly coupled system, consider the Fermi-velocity (see under equation (2.16)) $v_F = 3atc/(2\hbar)$. Note the factor of c and $\hbar$ not present under equations (2.16), since we wish to compare to the coupling constant for standard QED. Using the experimentally obtained values $t \approx 2.8eV$ and $a \approx 1.42\mathring{A}$ we obtain $v_F = c/300$. The coupling constant in QED is $\alpha_{\text{QED}} = e^2/(\hbar c) = 1/137$. For graphene, v_F replaces c

giving

$$\alpha = \frac{e^2}{\hbar v_F} = \frac{300e^2}{\hbar c} = 300\alpha_{\rm QED} \approx 2.2. \tag{2.29}$$

Any theory with $\alpha > 1$ is strongly coupled and inherently non-perturbative. In such a system, we cannot work with bare propagators and vertices.

2.2 Isotropic Integral Equations

We introduce dressing functions, which must then be determined using some non-perturbative technique. We will use Schwinger-Dyson (SD) equations. We describe below the basic structure of the method (further details are available in Appendix B). The dressed fermion propagator is defined as

$$\begin{aligned} S^{-1}(P) &= \left(S^{(0)}(P)\right)^{-1} + \Sigma(P) \\ &= i\gamma_\mu H^{\mu\nu}(P) M_{\nu\tau} P^\tau + D(P) \end{aligned} \tag{2.30}$$

where the bare propagator is obtained from equations (2.20), and (2.28) and

$$H^{\mu\nu} = \begin{bmatrix} Z & 0 & 0 \\ 0 & A & 0 \\ 0 & 0 & A \end{bmatrix}. \tag{2.31}$$

We note that if the theory were Lorentz invariant we would have $Z = A$. To write the dressed photon propagator we define the vector

$$n_\mu = \delta_{\mu 0} - \frac{p_0 P_\mu}{P^2} \tag{2.32}$$

and introduce four projection operators

$$P^1_{\mu\nu} = \delta_{\mu\nu} - \frac{P_\mu P_\nu}{P^2},\ P^2_{\mu\nu} = \frac{P_\mu P_\nu}{P^2},\ P^3_{\mu\nu} = \frac{n_\mu n_\nu}{n^2},\ P^4_{\mu\nu} = \frac{n_\mu P_\nu + n_\nu P_\mu}{p}. \tag{2.33}$$

Using this notation, the dressed inverse photon propagator is written

$$\begin{aligned} G^{-1}_{\mu\nu}(P) =& \frac{2}{\sqrt{P^2}} P^2 \left(P^1_{\mu\nu} + \frac{1}{\xi} P^2_{\mu\nu} \right) + \Pi_{\mu\nu}(P) \\ \Pi_{\mu\nu}(P) =& \alpha(P) P^1_{\mu\nu} + \beta(P) P^2_{\mu\nu} + \gamma(P) P^3_{\mu\nu} + \delta(P) P^4_{\mu\nu}. \end{aligned} \tag{2.34}$$

In order to satisfy gauge invariance we require that the polarization tensor is transverse (see the corresponding Ward-Takahashi identity $P^\mu \Pi_{\mu\nu} = 0$). Since $P^\mu P^2_{\mu\nu} \neq 0$ and $P^\mu P^4_{\mu\nu} \neq 0$ we must set $\beta = \delta = 0$. The remaining two projection operators are 4-D transverse: $P^\mu P^1_{\mu\nu} = P^\mu P^3_{\mu\nu} = 0$. We also note that $k_i P^3_{ij} = 0$ and $(k^2 \delta_{ij} - k_i k_j)(P^1_{ij} - P^3_{ij})$=0, from which we see that P^3_{ij} is 3-D transverse, and the combination $P^1_{ij} - P^3_{ij}$ is 3-D longitudinal. Inverting equation (2.34) and setting $\xi = 0$ we find the Landau-Gauge propagator

$$\begin{aligned} G_{\mu\nu} &= \frac{P^1_{\mu\nu} - P^3_{\mu\nu}}{G_T} + \frac{P^3_{\mu\nu}}{G_L} \\ G_L(P) &= 2\sqrt{P^2} + \alpha(P) + \gamma(P) \\ G_T(P) &= 2\sqrt{P^2} + \alpha(P)\,. \end{aligned} \tag{2.35}$$

The dressing functions, Z, A_1, A_2, D, α, and γ from equations (2.30) and (2.35) are obtained from solving the SD equations. The SD equations for the fermion self-energy and photon polarization tensor are found in Appendix B and are

$$\Sigma(P) = e^2 \int dK G_{\mu\nu}(Q) M^{\mu\tau} \gamma_\tau S(K) \Gamma^\nu \tag{2.36}$$

$$\Pi_{\mu\nu}(P) = -e^2 \int dK \mathrm{Tr}\left[S(Q) M_{\mu\tau} \gamma^\tau S(K) \Gamma_\nu \right] \tag{2.37}$$

where $Q^\mu = K^\mu - P^\mu$.

Ideally, the 3-vertex Γ should be found using its own SD equation (as outlined in Appendix B). However, vertex functions are numerically very difficult to calculate, and therefore we opt to use a well known [1, 3] truncation which preserves gauge invariance. The Ball-Chiu

vertex is

$$\Gamma_\mu = \frac{1}{2}\left(H^T_{\mu\nu}(P) + H^T_{\mu\nu}(K)\right)\gamma_\beta\, M^{\nu\beta} \tag{2.38}$$
$$+\left[\frac{1}{2}(P^\sigma + K^\sigma)\left(H^T_{\sigma\nu}(P) - H^T_{\sigma\nu}(K)\right)\gamma_\beta\, M^{\nu\beta} + i\left(D(P) - D(K)\right)\right]\frac{P_\mu + K_\mu}{P^2 - K^2}$$

where superscript T represents the transpose of the matrix. Using equations (2.30) and (2.38) it is easy to show that

$$iQ^\mu\Gamma_\mu = S^{-1}(P) - S^{-1}(K) \tag{2.39}$$

and therefore the Ward identity for the vertex function is satisfied. The last term in the Ball-Chiu vertex is difficult to deal with numerically, because both sub terms (H and D) go to $0/0 \to$ constant as $P \to K$. A common approximation is to drop this term [1], and this is what we do. To find self-consistent equations for the dressing functions Z, A, and D, we insert equation (2.38) into (2.36), multiply by the appropriate projection operators, and perform the trace in Dirac space. To find corresponding equations for the photon dressing functions α and γ, we insert equation (2.38) into (2.37), multiply by the required projection operators, and contract over Lorentz indices. Using the approximation $v_F \ll c$ we drop terms $\mathcal{O}(v_F^2)$ in the SD equation for the fermion self-energy, and find that only the G_L component of the photon propagator contributes. From equation (2.35) we see that this means we do not need to calculate α and γ individually, but only need the combination $\alpha + \gamma$. Using equations (2.33) and (2.34) we have

$$\Pi_{00}(P) = \frac{p^2}{P^2}\left(\alpha(P) + \gamma(P)\right) \tag{2.40}$$

and therefore we only need to calculate the 00 component of the photon polarization tensor. Using a more convenient notation, e.g. $Z(P) = Z_p$, the full set of self-consistent

integral equations we must solve are

$$
\begin{aligned}
Z_p &= 1 - \frac{2\alpha\pi v_F}{p_0}\int \frac{dK}{Q^2 S_k G_L}\, k_0 q^2 Z_k (Z_p + Z_k) \\
A_p &= 1 + \frac{2\alpha\pi v_F}{p^2}\int \frac{dK}{Q^2 S_k G_L}\left[q^2 A_k (Z_p + Z_k)\vec{k}\cdot\vec{p} + k_0 q_0 Z_k (Z_p + Z_k + A_p + A_k)\vec{p}\cdot\vec{q}\right] \\
D_p &= 2\alpha\pi v_F \int \frac{dK}{Q^2 S_k G_L}\, q^2 D_k (Z_p + Z_k) \\
\Pi_{00p} &= -16\pi v_F \alpha \int \frac{dK}{S_k S_q}\,(Z_k + Z_q)\left(A_k A_q v_F^2 (\vec{k}\cdot\vec{q}) + D_k D_q - k_0 q_0 Z_k Z_q\right)
\end{aligned}
\tag{2.41}
$$

where we have defined

$$S_k = k_0^2 Z_k^2 + v_F^2 k^2 + D_k^2 \tag{2.42}$$

$$G_L = \sqrt{Q^2} + \frac{Q^2}{q^2}(\Pi_{00q}). \tag{2.43}$$

2.3 Anisotropic Graphene

The insulating phase of graphene has never been seen experimentally. This is consistent with theoretical calculations which predict a range of critical couplings [1], but all greater than the maximum attainable coupling $\alpha_{\max} = 2.2$. The ability to produce the insulating phase would make graphene much more interesting technologically, and therefore research has been done on possible ways to create a gap. One possibility that is currently being studied is to produce a gap by straining graphene (either physically skewing the lattice or with an electromagnetic field). The authors of Ref. [16] introduced anisotropy by taking $v_{F_x} \neq v_{F_y}$ in matrix (2.20) and using a modified version of equation (2.31) of the form

$$H = \begin{bmatrix} Z & 0 & 0 \\ 0 & A_1 & 0 \\ 0 & 0 & A_2 \end{bmatrix} \tag{2.44}$$

with $A_1 \neq A_2$ in general. The set of coupled integral equations are

$$\begin{aligned}
Z_p =& 1 - \frac{2\alpha\pi v_F}{p_0}\int dK \frac{k_0 q^2 Z_k (Z_p + Z_k)}{Q^2 G_L S_k} \\
A_{1p} =& 1 + \frac{2\alpha\pi v_F}{p_x}\int dK \frac{q^2 A_{1k}(Z_p + Z_k)k_x + k_0 q_0 Z_k (Z_p + Z_k + A_{1p} + A_{1k})q_x}{Q^2 G_L S_k} \\
A_{2p} =& 1 + \frac{2\alpha\pi v_F}{p_y}\int dK \frac{q^2 A_{2k}(Z_p + Z_k)k_y + k_0 q_0 Z_k (Z_p + Z_k + A_{2p} + A_{2k})q_y}{Q^2 G_L S_k} \\
D_p =& 2\alpha\pi v_F \int dK \frac{q^2 D_k (Z_p + Z_k)}{Q^2 G_L S_k} \\
\Pi_{00p} =& -16\pi v_F \alpha \int \frac{dK}{S_k S_q}(Z_k + Z_q)(A_{1k}A_{1q}v_{Fx}^2 k_x q_x + A_{2k}A_{2q}v_{Fy}^2 k_y q_y + D_k D_q - k_0 q_0 Z_k Z_q)
\end{aligned} \tag{2.45}$$

where we have defined

$$G_L = \sqrt{Q^2} + \frac{Q^2}{q^2}(\Pi_{00q}) \tag{2.46}$$

$$S_k = k_0^2 Z_k^2 + A_{1k}^2 k_x^2 v_{Fx}^2 + A_{2k}^2 k_y^2 v_{Fy}^2 + D_k^2. \tag{2.47}$$

One major disadvantage of this formalism is that it does not reduce to the isotropic case in the limit that $v_{F_x} = v_{F_y}$, which can be seen immediately from (2.45). It is clear that setting $v_{Fx} = v_{Fy}$ and $A_1 = A_2$ on the right sides of (2.45) is not consistent with $A_1 = A_2$ on the left hand side, and neither A_1 or A_2 equal the isotropic A in equations (2.41. The isotropic limit does not produce the isotropic solution.

In order to simplify their numerical calculations, the authors of [16] set the first three fermion dressing functions to their bare limits ($Z = A_1 = A_2 = 1$), used a bare vertex instead of the Ball-Chiu ansatze in (2.38). They also used the 1-loop photon polarization tensor, obtained from the last line in equation (2.45) by setting $Z = A_1 = A_2 = 1$ and performing the integrations, which gives

$$\Pi_{00}^{1\,\text{loop}}(p_0, p_x, p_y) = \frac{\pi\alpha}{\sqrt{v_{Fx}v_{Fy}}} \frac{p_x^2 v_{Fx}^2 + p_y^2 v_{Fy}^2}{\sqrt{p_0^2 + p_x^2 v_{Fx}^2 + p_y^2 v_{Fy}^2}}. \tag{2.48}$$

At this level of approximation, the difficulty caused by the inconsistency described above becomes apparent. We will use the parameter $\eta = v_{Fy}/v_{Fx}$ to characterize the degree of anisotropy of the system. We can consider a range of values from $\eta = 1$, which corresponds to our original isotropic system, to $\eta \to 0$ which is maximally anisotropic. The hope is that large anisotropies, or small values of η will reduce the critical coupling, relative to the isotropic case.

$$\Pi_{00}^{1\,\mathrm{loop}} = \frac{\pi\alpha}{\sqrt{\eta}v_{Fx}} \frac{(p_x^2 + p_y^2\eta^2)v_{Fx}^2}{p_0^2 - (p_x^2 + p_y^2\eta^2)v_{Fx}^2} \tag{2.49}$$

The situation is further complicated by equation (2.48), since as $\eta \to 0$, Π_{00} increases in size and produces an artificially large screening effect, as emphasized in equation (2.49). This is part of the reason we wish to continue the project in the future using a less severe polarization tensor approximation.

We have reformulated the problem in a way that avoids the difficulties encountered in Ref. [16]. In our calculation we use

$$H = \begin{bmatrix} Z & 0 & 0 \\ 0 & A_1 & A_2 \\ 0 & -A_2 & A_1 \end{bmatrix} . \tag{2.50}$$

As we will show, our calculation is consistent in the sense that when $A_2 = 0$ and $v_{Fx} = v_{Fy}$ the set of self-consistent integral equations reduces to the isotropic equations (2.41) in section 2.1.

After applying the appropriate projection operators to equations (2.36) we obtain a set of coupled integral equations for five fermion dressing functions. Once again we find that the only part of the propagator (2.35) which contributes to the fermion self energy Σ is the longitudinal piece, G_L. We find therefore that, as before, we only need to calculate one component of the polarization tensor (see equation (2.40)). The set of integral equations

we will solve is

$$
\begin{aligned}
Z(P) &= 1 - \frac{2\alpha\pi v_F}{p_0}\int \frac{dK}{Q^2 S_k G_L} k_0 q^2 Z_k\,(Z_k + Z_p) \\
A_1(P) &= 1 + \frac{2\alpha\pi v_F}{p^2}\int \frac{dK}{Q^2 S_k G_L}\Big[k_0 q_0 Z_k(\vec{p}\cdot\vec{q})(A_{1k} + A_{1p} + Z_k + Z_p) \\
&\quad + q^2 A_{1k}(Z_k + Z_p)(\vec{k}\cdot\vec{p}) + k_0 q_0 Z_k(\vec{p}\times\vec{q}) - q^2 A_{2k}(Z_k + Z_p)(\vec{k}\times\vec{p})\Big] \\
A_2(P) &= \frac{2\alpha\pi v_F}{p^2}\int \frac{dK}{Q^2 S_k G_L}\Big[- k_0 q_0 Z_k(\vec{p}\times\vec{q})(A_{1k} + A_{1p} + Z_k + Z_p) \\
&\quad + q^2 A_{1k}(Z_k + Z_p)(\vec{k}\times\vec{p}) + k_0 q_0 Z_k(A_{2k} + A_{2p})(\vec{p}\cdot\vec{q}) + q^2 A_{2k}(Z_k + Z_p)(\vec{k}\cdot\vec{p})\Big] \\
D(P) &= 2\alpha\pi v_F \int \frac{dK}{Q^2 S_k G_L} q^2 D_k(Z_k + Z_p) \\
\Pi_{00}(P) &= -16\pi v_F \alpha \int \frac{dK}{S_k S_q}(Z_k + Z_q)\Big[D_k D_q - k_0 q_0 Z_k Z_q + A_{1k}A_{2q}(\vec{k}\times\vec{q})_v \\
&\quad A_{1q}A_{2k}(\vec{q}\times\vec{k})_v + A_{1k}A_{1q}(\vec{k}\cdot\vec{q})_v + A_{2k}A_{2q}(\vec{k}\cdot\vec{q})_{v'}\Big]
\end{aligned}
\tag{2.51}
$$

where we have defined

$$
S_k = k_0^2 Z_k^2 + v_{Fx}^2(k_x A_{1k} + k_y A_{2k})^2 + v_{Fy}^2(k_y A_{1k} - p_x A_{2k})^2 + D_k^2 \tag{2.52}
$$

and

$$
\begin{aligned}
\vec{k}\cdot\vec{p} &= k_x p_x + k_y p_y \\
(\vec{k}\cdot\vec{p})_v &= v_{Fx}^2 k_x p_x + v_{Fy}^2 k_y p_y \\
(\vec{k}\cdot\vec{p})_{v'} &= v_{Fy}^2 k_x p_x + v_{Fx}^2 k_y p_y \\
\vec{k}\times\vec{p} &= k_x p_y - k_y p_x \\
(\vec{k}\times\vec{p})_v &= v_{Fx}^2 k_x p_y - v_{Fy}^2 k_y p_x\,.
\end{aligned}
\tag{2.53}
$$

Note from equations (2.51-2.53) that if we take $A_2 \to 0$, and $v_{\mathrm{Fx}} \to v_{\mathrm{Fy}}$ we recover equations (2.41), with $A_1 = A$.

Chapter 3

Approximations

The main difficulty that arises in the numerical solution of Dyson-Schwinger equations is the size of the momentum phase space. It is common practice in the literature to reduce the complexity of numerical calculations by making some simplifying assumptions. Most of the commonly used approximations involve eliminating some dressing functions by using their perturbative forms, or ignoring the frequency dependence of some or all dressing functions. The hope in all cases is that a given approximation, although it may not produce physically accurate values of the critical coupling, will allow us to estimate the role of effects like anisotropy on the phase transition. Clearly this reasoning is potentially dangerous, since an approximation could remove or introduce competing effects that might change the result in unpredictable ways. We will describe some common approximations in the sections below, and explain which ones we adopt, and why.

3.1 One Dressing Function

Many calculations have been done by setting all fermion dressing functions except the gap to their bare values. A bare vertex, consistent with the Ward identity is used. While it may be possible to study qualitative effects this way, it is known that the renormalization of the Fermi velocity can produce a very large enhancement of the critical coupling [13].

3.2 Coulomb

The Coulomb approximation is very commonly used in condensed matter calculations. The idea is that since we have $v_F \ll c$, we know that the photons move much more quickly than the fermions. It is therefore a reasonable approximation to take $q_0 \to 0$, which means physically that we assume the interaction is instantaneous. It is easy to describe how this approximation works in the context of the isotropic calculation. The approximation results in three changes to the equations (2.41)

- The $k_0 q_0$ term in the Π_{00} equation (2.41) is set to 0
- Every factor of $\frac{q^2}{Q^2} \to 1$
- $G_L(Q) = 2\sqrt{Q^2} + \Pi_L(Q) \to 2q + \Pi_{00}(Q)$

3.3 Polarization Tensor Approximations

3.3.1 Non-Interacting

Calculations have been done in which the polarization tensor is simply set to zero.

3.3.2 1-Loop

It is also common to use a bare 1-loop polarization tensor instead of calculating Π_{00} self-consistently. The argument in this case is based on the vanishing density of states at the Dirac points, which indicates that using bare lines in the photon self-energy should be a reasonable approximation. The 1-loop result is given in equation (2.48) for the anisotropic case, the analogous expression for the isotropic expression can be obtained from setting $v_{Fx} = v_{Fy} = v_F$.

3.3.3 Instantaneous

The fully instantaneous limit is $\Pi_{00}(q_0, q_1, q_2) \to \Pi_{00}(0, q_1, q_2)$. This is usually used in combination with the Coulomb approximation, where it is assumed the frequency dependence can be neglected. However, previous calculations indicated that using a fully back-coupled polarization tensor results in a significant reduction of the critical coupling [2].

3.4 GGG

One particularly convenient combination of these approximations is the Gamayun-Gorbar-Guysin (GGG) approximation. The first part of the approximation is that they use the idea from section 3.1, and worked with only one dressing function which is obtained from the second last line in equation (2.41). They also apply the Coulomb approximation of section 3.2. The integral equation for the gap function is

$$D_p = 4\pi\alpha v_F \int dK \, \frac{D_k}{(2q + \Pi_{00}(k_0, q_1, q_2)) \left(D_k^2 + v_{\mathrm{Fx}}^2 k_1^2 + v_{\mathrm{Fy}}^2 k_2^2 + k_0^2\right)} \,. \tag{3.1}$$

For Π_{00}, they use (2.48) in the isotropic instantaneous limit. The k_0 integral can be done analytically. The result is

$$D(p_1, p_2) = \alpha v_F \int \frac{dk_1}{2\pi} \int \frac{dk_2}{2\pi} \frac{J(B, g) D_k}{q\sqrt{q_x^2 v_{\mathrm{Fx}}^2 + q_y^2 v_{\mathrm{Fy}}^2}} \tag{3.2}$$

$$J(B, g) = \frac{(B^2 - 1)\left[\pi - g f(B)\right] + B g^2 f(g)}{B\left(B^2 + g^2 - 1\right)} \tag{3.3}$$

$$f(x) = \begin{cases} \frac{2\cos^{-1}(x)}{\sqrt{1-x^2}} & \text{if } x < 1 \\ 2 \text{ if } x = 1 \\ \frac{2\cosh^{-1}(x)}{\sqrt{x^2-1}} & \text{if } x > 1 \end{cases} \tag{3.4}$$

$$B = \sqrt{\frac{D_k^2 + v_F^2\left(\eta k_x^2 + \frac{k_y^2}{\eta}\right)}{v_F^2\left(\eta q_x^2 + \frac{q_y^2}{\eta}\right)}} \quad \text{and} \quad g = \frac{\pi\alpha\sqrt{\eta q_x^2 + \frac{q_y^2}{\eta}}}{2q} \tag{3.5}$$

3.5 Vertex Ansätze

For calculations which consider non-zero dressing functions, vertex corrections are needed to satisfy gauge invariance. We give a brief discussion of the most general construction of vertex dressing functions. We consider a general decomposition of the vertex function, which we denote $\Gamma(P, K)$ where P denotes the momentum of the incoming fermion, and K is the momentum of the outgoing fermion. The incoming photon momentum is written $Q = K - P$. We consider a general decomposition of the vertex function (a detailed description can be found in [6]). We start by constructing the basis vectors. There are three available vectors, γ^μ, K^μ, P^μ and four spinor scalars 1, $\not{K}$, $\not{P}$, $\not{K}\not{P}$. Combining these structures gives us 12 different basis vectors. We want to construct a vertex which satifies the Ward-Takahashi and the Ward Identity, which are respectively:

$$iQ_\mu \Gamma^\mu(P, K) = S^{-1}(P) - S^{-1}(K) \tag{3.6}$$

$$\Gamma^\mu(P, P) = i\frac{\partial}{\partial P^\mu} S^{-1}(P). \tag{3.7}$$

First we note that since the fermion propagator contains no $\not{P}\not{K}$-like terms (see equation (2.30)), we must set the dressing functions for these basis vectors to 0, in order to ensure equations (3.6) and (3.7) are satisfied. The remaining structures can be grouped together into forms that are either longitudinal or transverse with respect to the photon momentum Q. The transverse part satisfies:

$$Q_\mu \Gamma^\mu_T(K,P) = 0 \tag{3.8}$$

$$\Gamma^\mu_T(P,P) = 0. \tag{3.9}$$

This means only the longitudinal component is constrained by the equations (3.6) and (3.7). The transverse component is therefore not determined by the requirement that the vertex should satisfy the Ward identity. The contribution of the transverse components is generally believed to be small [3]. We therefore simply set the transverse part to zero. If we write the fermion propagator as

$$S^{-1}(P) = -iF(P^2)\not{P} + D(P^2) \tag{3.10}$$

then we can represent a longitudinal vertex, which satisfies equations (3.6) and (3.7), as:

$$\begin{aligned}\Gamma^\mu_L(P,K) &= \frac{\gamma^\mu}{2}\left[F(P)+F(K)\right] \\ &+ \left[\frac{1}{2}(\not{P}+\not{K})\left[F(P)-F(K)\right] + i(D(P)-D(K))\right]\frac{(P+K)^\mu}{P^2-K^2}.\end{aligned} \tag{3.11}$$

Equations (3.10, 3.11) are the isotropic and Lorentz invariant version of (2.30, 2.38).

Chapter 4

Numerical Methods and Code

The numerical part of the research presented in this thesis is to solve the set of coupled integral equations in equation (2.51). Most of our calculations were done using the 1-loop approximation for the photon polarization tensor which is given in equation (2.48). In the subsections below we discuss various aspects of the numerical formulation of the problem.

4.1 Integral Bounds

We remind the reader that we have defined the notation

$$dK = \frac{d^3k}{(2\pi)^3} = \int_{-\infty}^{\infty} \frac{dk_0}{2\pi} \int_0^{\infty} \frac{dk}{2\pi}\, k \int \frac{d\theta_k}{2\pi}. \tag{4.1}$$

The integration region for the k_0 and k integrals are infinite, but numerically we must use finite bounds. This is justified if the theory is properly renormalized, in which case all integrals are ultra-violet finite. In general, the renormalization of a gauge theory is highly non-trivial, but since we are working in 3-D renormalization is simple. The only divergence occurs in the photon polarization tensor, and can be removed by a simple subtraction. We define $\Pi^R_{\mu\nu}(P) = \Pi_{\mu\nu}(P) - \Pi_{\mu\nu}(0)$ which satisfies the renormalization condition $\Pi^R_{\mu\nu}(0) = 0$. This renormalization is performed in all numerical calculations,

and the subscript R is suppressed. We use a cutoff Λ on the momentum integrals, and scale the dimensionful dressing functions by the appropriate power of Λ to remove all dependence on the cutoff. We illustrate this using as an example the integral equation for the dressing function D in the third line of (2.41). We define dimensionless variables

$$\hat{p} = \frac{p}{\Lambda},\ \hat{p}_0 = \frac{p_0}{\Lambda},\ \hat{k} = \frac{k}{\Lambda},\ \hat{k}_0 = \frac{k_0}{\Lambda} \tag{4.2}$$

$$\hat{D}_p = \frac{D_p}{\Lambda},\ \hat{S}_{\hat{k}} = \frac{S_k}{\Lambda^2} \tag{4.3}$$

$$\hat{G}_L = \frac{G_L}{\Lambda},\ \hat{\Pi}_{00p} = \frac{\Pi_{00p}}{\Lambda}. \tag{4.4}$$

In terms of these variables, the integral equation becomes

$$\Lambda\hat{D}_p = \Lambda^3 \int_0^1 d\hat{k}_0 \int_0^1 d\hat{k} \int_0^{2\pi} d\theta\hat{k} \frac{\Lambda^2\hat{q}^2\Lambda\hat{D}_k(Z_p + Z_k)}{\Lambda^2\hat{Q}^2\Lambda\hat{G}_L\Lambda^2\hat{S}_k} \tag{4.5}$$

from which we see that all factors of Λ cancel and we obtain

$$\hat{D}_p = \int_0^1 d\hat{k}_0 \int_0^1 d\hat{k} \int_0^{2\pi} d\theta\hat{k}\hat{D}_{\text{int}}(\hat{p}_0, \hat{p}, \hat{k}_0, \hat{k}) \tag{4.6}$$

where $\hat{D}_{\text{int}}$ is the integrand which is a function of only hatted variables. In all numerical calculations, we use the hatted variables. The critical coupling (α_c) is the value of α for which $\hat{D}_p(0,0)$ goes to zero. From this point onward, all the hats will be suppressed.

4.2 Phase Space

We used Fortran 08 as our language of choice to solve the system of coupled equations (2.51). The integrals over momentum space were discretized in a standard way, using Gauss-Legendre quadrature. To determine what resolution we used (the size of the partitions across momentum space), we increased the number of points until the dressing functions stopped changing to a specified level of numerical accuracy. A logarithmic scale was employed in order to increase the number of lattice points close to the origin,

and therefore close to the region of the equations which we were most concerned with (the zero-momentum values). Gauss-Legendre quadrature was employed in choosing the points of the lattice, further increasing the point density around the origin, and increasing the overall accuracy of the discretized integrals compared to a constant partitioning.

4.3 Interpolation

Our equations are self-consistent, so we obtain solutions with an iterative procedure. We start with an initial guess for the values of the dressing functions, and put them into the right hand side of equations (2.51). After all integrations have been done, output values of the dressing functions are obtained. The calculation is repeated, using the output functions as input on the right hand side, and producing new output functions. The procedure is repeated until the output functions match the input functions (to the specified numerical accuracy), which indicates that a solution of the set of integral equations has been found.

The structure of the integrands requires interpolation. This happens because the integrands depend on the dressing functions evaluated at values of $Q = K - P$, but the previous integration gives the dressing functions only at the originally chosen grid points for the external variables P. Interpolation is both time consuming and a source of error. After experimentation with several different methods, we determined that the best method for our problem is simple linear interpolation. Our dressing functions depend on three independent arrays, and therefore we need 3-D linear interpolation. We describe this process below. The external variables are p_0, p, θ_p and the internal integration variables are k_0, k, θ_k. We also use $\vec{q} = \vec{k} - \vec{p}$, and therefore

$$\begin{aligned} |q| &= \sqrt{q_1^2 + q_2^2} \\ &= \sqrt{(k_1 - p_1)^2 + (k_2 - p_2)^2} \\ &= \sqrt{(k\cos\theta_k - p\cos\theta_p)^2 + (k\sin\theta_k - p\sin\theta_p)^2}. \end{aligned} \tag{4.7}$$

The angle θ_q is defined through the equation

$$\vec{q} = (q\cos\theta_q, q\sin\theta_q) \tag{4.8}$$

and θ_q is related to the values of θ_p and θ_k using a straightforward trigonometric relation

$$q_1 = k\cos\theta_k - p\cos\theta_p,\ \ q = |k-p|,\ \ \theta_q = \arccos(q_1/q). \tag{4.9}$$

We have, from the previous iteration, an array of numbers that give the values of our functions $Z(p_0, p, \theta_p)$, $A_1(p_0, p, \theta_p)$, $A_2(p_0, p, \theta_p)$ and $D(p_0, p, \theta_p)$ at the values of our external grid points. In order to perform the next iteration, we need the values of these dressing functions at the point (q_0, q, θ_q), which necessitates interpolation. The time consuming part of the process is the search algorithm that identifies the three pairs of indices that correspond to the points in the 3-D domain that bracket the point (q_0, q, θ_q) at which we want to know the values of our dressing functions. We describe below how this interpolation is done using a section of pseudo-code.

```
1  do p0 = 1,MM
2  do p = 1,NN
3  do thetap=1,NNtheta
4  do k0=1,MM2
5          q0=k0-p0
6
7  !find the indices i1 and i2 so that
8  !p0array(i1) < q0 < p0array(i2) and save these indices
9
10 do k=1,NN2
11 do thetak=1,NNtheta
12         q = dsqrt((k cos{thetak} - p cos{thetap})^2 + (ksin{thetak} &
13         - psin{thetap})^2)
14
```

```
15 !find the indices j1 and j2 so that parray(j1) < q < parray(j2)
16
17 !find the indices k1 and k2 so that
18 !xarray(k1) < \cos(thetak) < xarray(j2)
19
20 !input the indices (i1,i2,j1,j2,k1,k2) into the
21 !interpolater subroutine, which outputs the
22 !interpolated value of our dressing functions,
23 !for example A(q0,q,thetaq)
24
25 end do
26 end do
27 end do
28 end do
29 end do
30 end do
```

Lines 7-8 are a customized "pre-interpolation" step that allow us to save time by performing the first index search outside of the two innermost loops. The thetaq in line 23 is obtained from equation (4.9).

4.4 Adaptive Grid

The integrals that give the fermion dressing functions are numerically unstable because there is a singularity in the integrands when the integration variables K are equal to the external variables P. This is not caused by the anisotropy, but is a common feature of the isotropic calculation, and both anisotropic calculations we have discussed. The problem is caused by the factor $1/Q^2 = 1/(K-P)^2$ in the equations for the fermion dressing functions (see equations (2.41), and (2.51)). The singularity is integrable, but

it must be dealt with carefully in a numerical calculation. Our method is as follows. We consider the example of the k_0 integral. The integral is calculated in two pieces $\int_0^{\Lambda} dk_0 = \int_0^{p_0} dk_0 + \int_{p_0}^{\Lambda} dk_0$. Since we have divided the integration range at the singular point p_0, and since Gauss-Legendre is an open integration method that does not use grid points at the exact values of the ends of the integration range, there is no divergent contribution to the numerical integral. In order to obtain a numerically accurate result, the total number of grid points are divided between the two pieces as follows. We use N_1 points in the first piece, and $N_2 = M - N_1$ points in the second piece. The k_0 array for piece 1 is $(k_{0min1}, ...k_{0max1})$ and for piece 2 it is: $(k_{0min2}, ...k_{0max2})$. The values of the points in these arrays are determined from the Gauss-Legendre integration algorithm and depend on the value of N_1 (and N_2). In a separate internal loop, N_1 is stepped from 1 to $M-1$ until the value $N_{1\text{best}}$ is found for which $|(p_0 - k_{0max1}) - (k_{0min2} - p_0)|$ is minimum. The result is that when we divide the integral so that there are $N_{1\text{best}}$ points in the lower half, and $M - N_{1\text{best}}$ points in the upper half, the singularity in between the two pieces is approached symmetrically from each side. Our algorithm is efficient because the extra time required to find $N_{1\text{best}}$ is more than compensated for by allowing us to obtain a convergent result for the integral with a much smaller value of M.

Chapter 5

Results

For the purposes of this thesis, we choose to focus mostly on our "1-loop Π" approximation results, as the "back-coupled" calculations are still in progress. In figures 5.1-5.4 we show the fermion dressing functions for one value of coupling ($\alpha = 4$ which is greater than the critical coupling) and two different values of the anisotropy parameter. We use $\eta = 1$, which is the value for which our equations reduce to the isotropic ones, and $\eta = 0.65$. We display cross-sections of the 3-D phase space. Each graph has four curves, which are obtained by holding either p_0 or p fixed, at either its maximum or minimum value (we remind the reader that using our scaled variables, the maximum value of any momentum variable is 1 - see section 4.1). For the dressing functions Z and A_1, the change produced when η is reduced from 1 to 0.65 is too small to see on the graph, and therefore Fig. 5.1(b) shows the relative difference $(Z_{\eta=1} - Z_{\eta=0.65})/(Z_{\eta=1} + Z_{\eta=0.65})$, and the Fig 5.2(b) shows the same relative difference for A_1. The angular dependence of all the dressing functions is very weak. We note the following features from these results.

- At high momentum, all dressing functions approach the perturbative limit (Z, A_1 go to 1, and D and A_2 go to zero). This verifies that we recover the perturbative limit at high momentum.

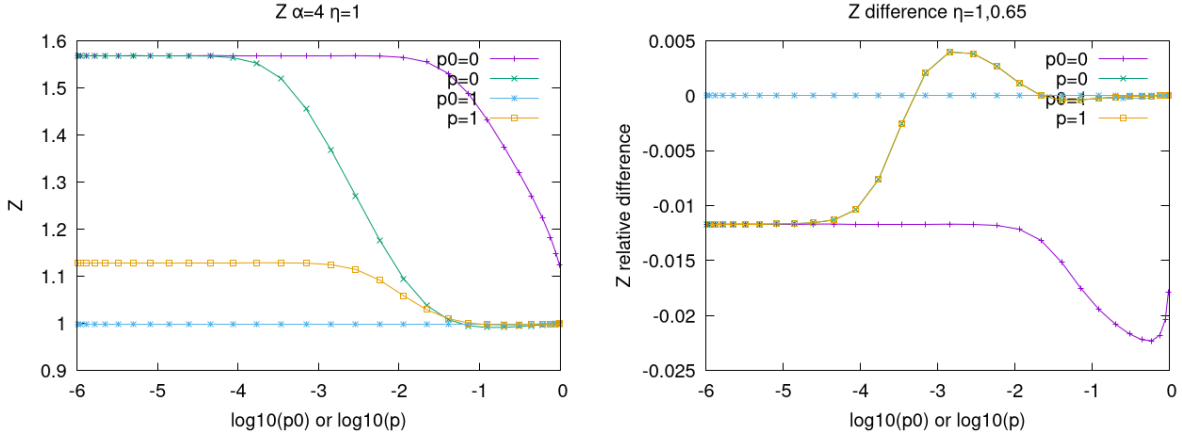

(a) 1 loop Z

(b) 1 loop Z difference between $\eta = 1$ and $\eta = 0.65$

FIGURE 5.1: Z dressing function obtained using the 1-loop approximation for Π, for four different cross-sections of the momentum phase space

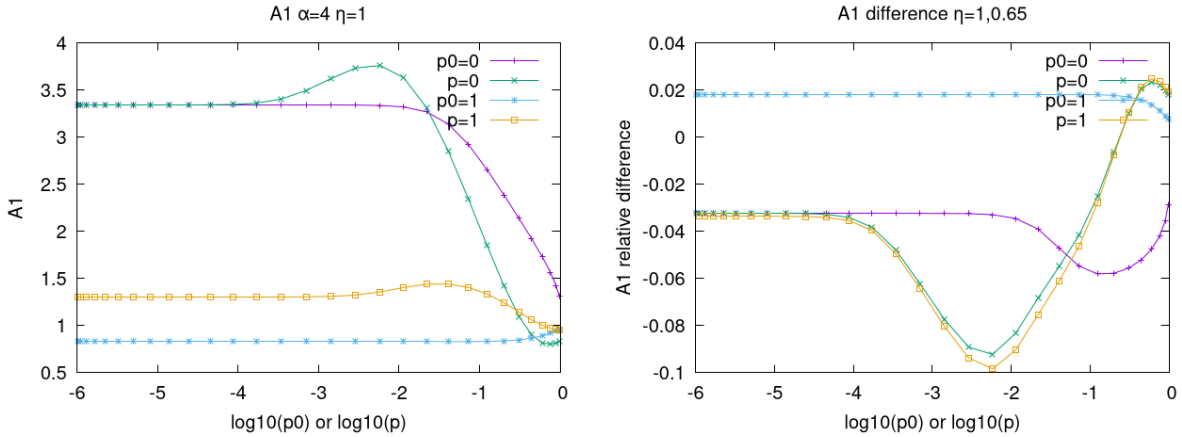

(a) 1 loop A_1

(b) 1 loop A_1 difference between $\eta = 1$ and $\eta = 0.65$

FIGURE 5.2: A_1 dressing function obtained using the 1-loop approximation for Π, for four different cross-sections of the momentum phase space

- Fig. 5.3 shows the dressing function A_2 at $\eta = 0.85$ and $\eta = 0.65$. At $\eta = 1$, where this dressing function should be identically zero, we have $\text{Max}|A_2(p_0, p, \theta_p)| \approx 10^{-5}$, which demonstrates the numerical accuracy of our calculation.

- At low momenta the values of Z and A_1 are significantly enhanced (especially A_1), which shows that the approximation discussed in section 3.1 cannot be expected to produce reliable results. As the coupling is reduced, this enhancement becomes more pronounced.

- Increasing anisotropy lowers D, which will increase the value of the critical coupling.

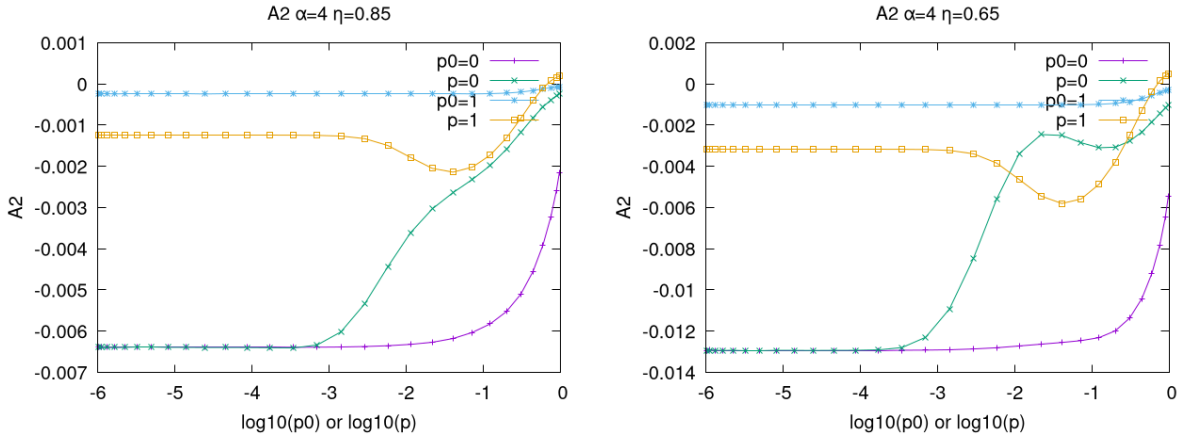

(a) 1 loop A_2 $\eta = 0.85$ (b) 1 loop A_2 $\eta = 0.65$

FIGURE 5.3: A_2 dressing function obtained using the 1-loop approximation for Π, for four different cross-sections of the momentum phase space

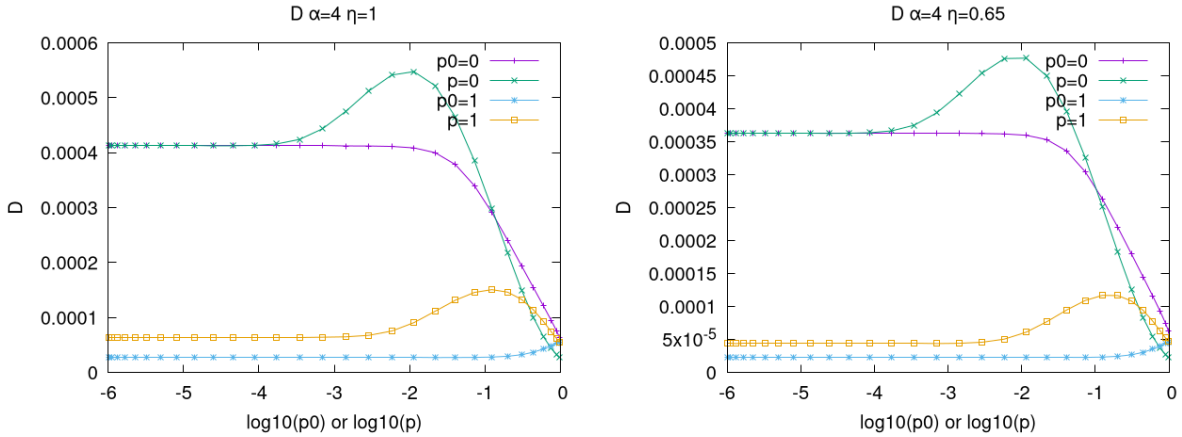

(a) 1 loop D, $\eta = 1$ (b) 1 loop D, $\eta = 0.65$

FIGURE 5.4: D dressing function obtained using the 1-loop approximation for Π, for four different cross-sections of the momentum phase space

In Fig. 5.5 we show the Fermi velocity defined as

$$v_F = \frac{\sqrt{A_1^2 + A_2^2}}{Z} \tag{5.1}$$

versus p with $p_0 = 0$. The four curves show $\eta = 1$ and $\eta = 0.65$ for $\alpha = 4$ and $\alpha = 3.59$. The experimentally observed increase in the Fermi velocity at small coupling is clearly seen. As the anisotropy increases, the effect is reduced. We see the experimentally observed increase of the Fermi velocity below the critical coupling, just as in figure 4 of [2]

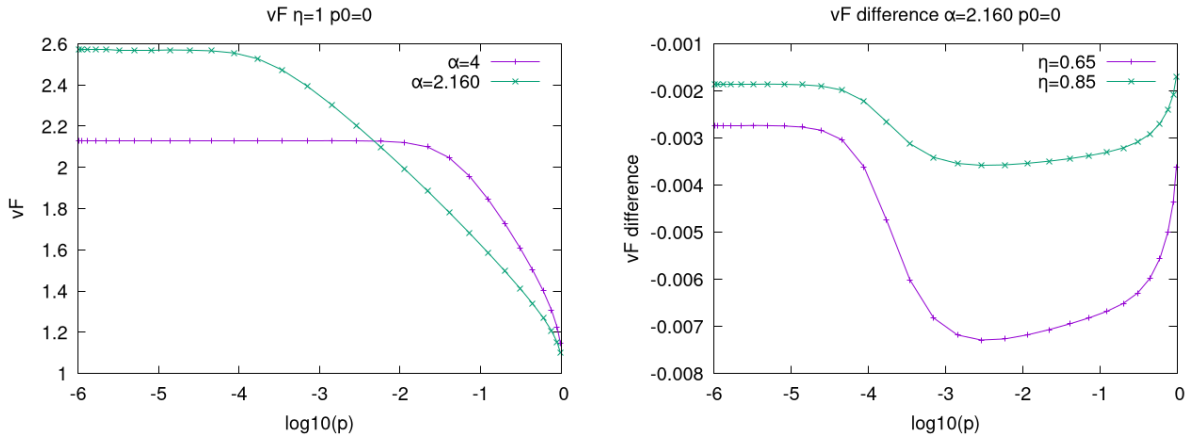

FIGURE 5.5: The renormalized Fermi velocity for two values of η and two values of coupling

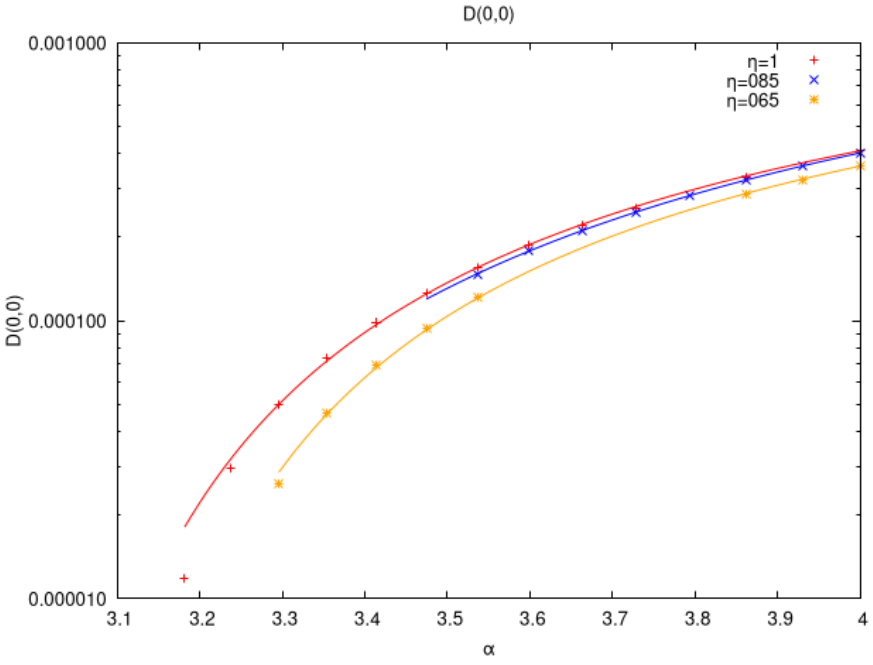

FIGURE 5.6: The condensate $D(0)$ vs. coupling for different values of the anisotropy parameter

In Fig. 5.6 we show the value of the condensate $D(0)$ versus coupling, for three different values of the anisotropy parameter. One sees that anisotropy suppresses the condensate, and therefore increases the critical coupling. This is consistent with what we see in Figs. 5.2 and 5.5, which show that the dominant effect of anisotropy is an enhancement of A_1 and the fermi-velocity, which can be expected to suppress the formation of a condensate.

In our calculation we have used only three approximations.

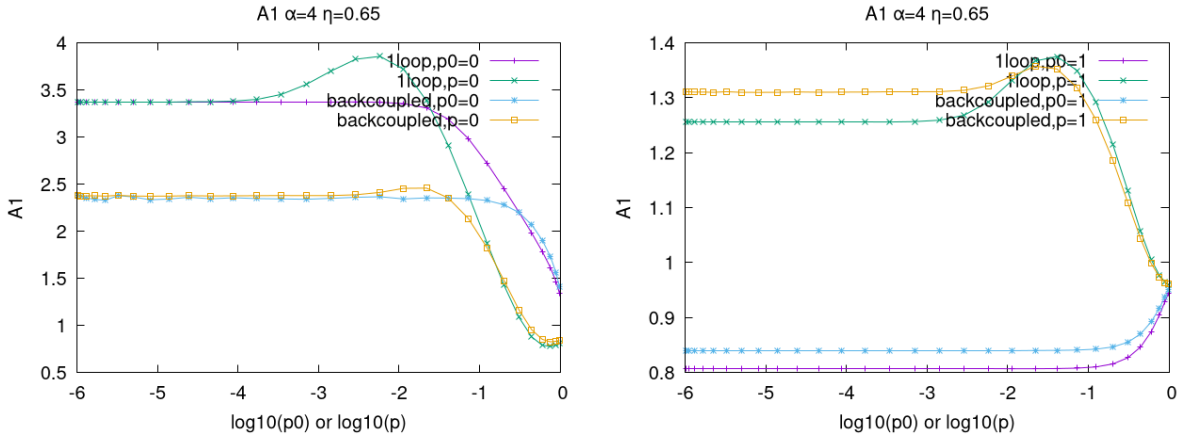

(a) $p_0 = 0$ and $p = 0$ for 1loop and backcoupled A_1

(b) $p_0 = 1$ and $p = 1$ for 1loop and backcoupled A_1

FIGURE 5.7: The dressing function A_1 for $\eta = 0.65$ and $\alpha = 4$, for the backcoupled and 1-loop calculations

- We have assumed $v_F \ll c$, which is physically well justified.

- We have used the first term of the Ball-Chiu ansatz for the vertex function (see section 3.5). This approximation is known to be very good in the isotropic case [1].

- We have used the 1-loop photon polarization tensor (see section 3.3.2). This approximation is likely the most problematic, and we have already begun calculations on the fully 'back-coupled' calculation in which all five equations in (2.51) are solved self-consistently. In Fig. 5.7 we show some preliminary results from that calculation. The figure shows clearly that the dressing function A_1, which we have seen to play an important role in the formation of the gap function, is suppressed relative to the results obtained from the 1-loop approximation.

Chapter 6

Conclusions

We have calculated the critical coupling at which the semi-metal to insulator transition occurs in graphene using a low energy effective theory. We have studied the effect of anisotropy on the phase transition, which could be introduced as physical strain on the graphene lattice, or as an applied magnetic field. We have included anisotropy by considering a Fermi velocity which is not isotropic in space ($v_{Fx} \neq v_{Fy}$). There are several previous calculations in the literature that attempted something similar [15, 16] but introduced numerous restrictive assumptions to make the numerical calculation more tractable. The effect of these approximations is difficult to predict, and in fact different approximations have lead to predictions that the critical coupling in an anisotropic system moves in different directions, relative to the isotropic one. Our calculation includes the complete non-perturbative fermion propagator, coupled to a 1-loop polarization tensor through a set of Schwinger-Dyson (SD) equations. The hierarchy of SD equations are truncated using a Ball-Chiu vertex ansatz. Full frequency dependence of the dressing functions is included. Numerically the calculation involves 6 nested loops, $30 * 30 * 18 = 1.62 * 10^4$ internal points $100 * 100 * 50 = 5 * 10^5$ external points for a total phase space of $8.1 * 10^9$ grid points. Sufficient numerical speed is achieved by parallelizing using openMPI 4.0.1. Our results show that the effect of anisotropy is much smaller than that predicted by previous calculations, and that it increases the critical coupling from 3.14 in the isotropic

case, which agrees fairly well with [1], to ≈ 3.21 when $\eta = 0.65$. These values are based on extrapolation from the data in figure 5.6 using a fitting tool from Mathematica. We compared our extrapolation across three different methods (see [1]).

The most important approximation we have made is the use of a 1-loop photon polarization tensor. This approximation is justified by the vanishing electron density of states at the Dirac points, close to which the low energy effective theory is valid. However, it is known that, in an isotropic calculation, the critical coupling is reduced when the polarization tensor is calculated self-consistently from its own SD equation. It is therefore important to perform the fully back-coupled calculation in the anisotropic case. This calculation is currently in progress.

The value of the critical coupling produced by any calculation based on an effective theory is not expected to be exact, since there are potentially important screening effects that are necessarily ignored. The point of the calculation is to establish whether or not anisotropy could reduce the critical coupling, and therefore make it experimentally possible to produce an insulating state. Our 1 loop results indicate that the critical coupling is moving in the wrong direction, but this could change when we solve the full set of back coupled equations.

Appendix A

Propagators

The Euclidean action in 3-D for graphene is given by

$$S = \int d^3x \sum_a \bar{\psi}_a \left(i\partial_\mu - eA_\mu\right) M^{\mu\nu}\gamma_\nu\psi_a + \tfrac{1}{2}F_{\mu\nu}\tfrac{1}{\sqrt{-\partial^2}}F^{\mu\nu} + \text{gauge fixing.} \tag{A.1}$$

$$\tag{A.2}$$

A.1 Fermion

We will begin with the bare fermion propagator. Since we only want the propagator, we will set the interacting term in equation (A.1) to 0. The Euler-Lagrange equation for ψ is

$$\frac{\partial\mathcal{L}}{\partial\overline{\psi}} = 0 \tag{A.3}$$

$$i\partial_\mu M^{\mu\nu}\gamma_\nu\psi(x) = 0. \tag{A.4}$$

The Green's function for this equation of motion satisfies

$$i\partial_\mu M^{\mu\nu}\gamma_\nu S_F(x-x') = \delta^4(x-x'). \tag{A.5}$$

Taking the Fourier Transform we obtain the bare fermion propagator as

$$iP_\mu M^{\mu\nu}\gamma_\nu S_F(P) = \int d^4P\delta^4(P) = 1$$

$$S_F(P) = -i\left[P_\mu M^{\mu\nu}\gamma_\nu\right]^{-1}. \tag{A.6}$$

A.2 Photons

Since we only want the propagator, we will set the interacting term in equation (A.1) to 0. We start with the Euler-Lagrange equation, but this time in terms of the electromagnetic four-potential

$$\partial_\mu\left(\frac{\partial\mathcal{L}}{\partial(\partial_\mu A_\nu)}\right) = 0. \tag{A.7}$$

We define an operator $\hat{L}$ as follows

$$\hat{L}_{\mu\nu} = \left(\delta_{\mu\nu}\partial_\rho\partial^\rho - \partial_\mu\partial_\nu + \frac{1}{\xi}\partial_\nu\partial_\mu\right) \tag{A.8}$$

in terms of which the Euler-Lagrange equation is

$$\hat{L}_{\mu\nu}A^\mu = 0. \tag{A.9}$$

The Green's function or propagator for the photon is

$$\hat{L}_{\mu\nu}G^{\mu\nu}(x-x') = \delta(x-x'). \tag{A.10}$$

Taking the Fourier transform we obtain

$$\left(\delta_{\mu\nu}P^2 - P_\mu P_\nu + \frac{1}{\xi}P_\mu P_\nu\right)G^{\mu\nu}(P) = 1. \tag{A.11}$$

Inverting the operator gives

$$G^{\mu\nu}(P) = \frac{1}{P^2}\left(\delta^{\mu\nu} + (\xi - 1)\frac{P^\mu P^\nu}{P^2}\right). \tag{A.12}$$

A.3 Vertex

The Feynman rule for the vertex can be obtained from the interacting term in the Lagrangian. We obtain

$$\Gamma_\mu(P, K) = -eM_{\mu\nu}\gamma^\nu. \tag{A.13}$$

One can verify that this vertex, together with equation (A.6) satisfies the Ward identity

$$iQ_\mu\Gamma^\mu(P, K) = S^{-1}(K) - S^{-1}(P). \tag{A.14}$$

Appendix B

Schwinger-Dyson Equations

The Schwinger-Dyson equations are a standard tool to include non-perturbative effects in quantum field theories.

To understand the Dyson-Schwinger scheme, we start with the standard QED action

$$S[\overline{\psi}, \psi, A_\mu] = \int d^4x \left[\overline{\psi} \left(i\partial\!\!\!/ - m + eA\!\!\!/ \right) \psi - \frac{1}{4} F_{\mu\nu} F^{\mu\nu} - \frac{1}{2\xi} \left(\partial_\mu A^\mu \right)^2 \right]. \tag{B.1}$$

The corresponding generating functional is

$$Z[\overline{\eta}, \eta, J_\mu] = \int d\mu \exp\left(iS[\overline{\psi}, \psi, A_\mu] + i \int d^4x \left[\left(\bar{\psi}\eta + \bar{\eta}\psi \right) + A_\mu J^\mu \right] \right) \tag{B.2}$$

where $d\mu = \mathcal{D}\bar{\psi}\mathcal{D}\psi\Pi_\mu \mathcal{D}A_\mu$ is the measure of the functional integral. The generating functional includes source terms for each of the constituent fields of the theory, here η for the fermion, $\bar{\eta}$ for the anti-fermion, and J^μ for the photon. The equations of motion for the fields are obtained using functional derivatives. The Schwinger-Dyson equations are obtained from the idea that taking the integral of the total functional derivative of the partition function with respect to any field gives zero, assuming appropriate boundary

conditions. Differentiating with respect to the photon field gives

$$\begin{aligned} 0 &= \int d\mu \frac{\delta}{\delta A_\mu(x)} \exp\left(iS + i\int d^4x \left[(\bar{\psi}\eta + \bar{\eta}\psi) + A_\mu J^\mu\right]\right) \\ &= \int d\mu \left(\frac{\delta S}{\delta A_\mu(x)} + J_\mu(x)\right) \exp\left(iS + i\int d^4x \left[(\bar{\psi}\eta + \bar{\eta}\psi) + A_\mu J^\mu\right]\right) \\ &= \left(\frac{\delta S}{\delta A_\mu(x)}\left[\frac{\delta}{i\delta J}, \frac{\delta}{i\delta\overline{\eta}}, -\frac{\delta}{\delta\eta}\right] + J_\mu(x)\right) Z. \end{aligned} \tag{B.3}$$

We can write this in a more convenient way by defining a new function $\mathcal{G}$ as:

$$Z(J, \eta, \bar{\eta}) = \exp \mathcal{G}(J, \eta, \bar{\eta}) \tag{B.4}$$

so that e.g. $\frac{\delta Z}{\delta J(x)} = Z\frac{\delta \mathcal{G}}{\delta J(x)}$. Equation (B.3) becomes

$$0 = \left(\partial_\rho\partial^\rho g_{\mu\nu} - \left(1 - \frac{1}{\xi}\right)\partial_\mu\partial_\nu\right)\frac{\delta\mathcal{G}}{i\delta J_\nu(x)} + \frac{\delta\mathcal{G}}{\delta\eta}\gamma_\mu\frac{\delta\mathcal{G}}{\delta\overline{\eta}} + \gamma_\mu\frac{\delta^2\mathcal{G}}{\delta\eta\delta\overline{\eta}} + J_\mu(x). \tag{B.5}$$

The generating functional for 1 particle irreducible n-point functions is obtained from a Legendre transform

$$\Gamma[\bar{\psi}, \psi, A_\mu] = i\mathcal{G}[\bar{\eta}, \eta, J_\mu] + i\int d^4x \left[\bar{\psi}\eta + \bar{\eta}\psi + A_\mu J^\mu\right]. \tag{B.6}$$

The functional derivatives of this generating functional are the sources

$$\begin{aligned} J_\mu(x) &= -\frac{\delta\Gamma}{\delta A_\mu(x)} \\ \eta(x) &= -\frac{\delta\Gamma}{\delta\overline{\psi}(x)} \\ \bar{\eta}(x) &= \frac{\delta\Gamma}{\delta\psi(x)}. \end{aligned} \tag{B.7}$$

From equations (B.2) and (B.4) we obtain convenient expressions for the fields (1 point

functions) in the theory in terms of functional derivatives with respect to their corresponding sources.

$$\begin{aligned} A_\mu =& \frac{1}{i}\frac{\delta \mathcal{G}}{\delta J_\mu(x)} \\ \psi(x) =& \frac{1}{i}\frac{\delta \mathcal{G}}{\delta \bar{\eta}(x)} \\ \bar{\psi}(x) =& -\frac{1}{i}\frac{\delta \mathcal{G}}{\delta \eta(x)}. \end{aligned} \tag{B.8}$$

Additional functional derivatives give higher order n-point function for the theory. Note that

$$-\delta_{\alpha\beta}\delta^4(x-y) = \frac{1}{i}\int d^4z \frac{\delta^2 \mathcal{G}}{\delta\eta_\alpha(x)\delta\overline{\eta}_\gamma(z)}\frac{\delta^2\Gamma}{\delta\psi_\gamma(z)\overline{\psi}_\beta(y)}\Big|_{\eta=\overline{\eta}=\psi=\overline{\psi}=0}. \tag{B.9}$$

Using this, we may insert the definitions from equations (B.7) and (B.8) into equation (B.5), we obtain

$$\frac{\delta\Gamma}{\delta A^\mu(x)}\Big|_{\psi=\overline{\psi}=0} = \left(\partial_\rho\partial^\rho g_{\mu\nu} - (1-\frac{1}{\xi})\partial_\mu\partial_\nu\right)A^\nu(x) - iTr\left[\gamma_\mu\left(\frac{\delta^2\Gamma}{\delta\overline{\psi}\delta\psi}\right)^{-1}(x,x)\right]. \tag{B.10}$$

The 2-point functions, or the propagators, for the fermion and boson fields are, respectively

$$\begin{aligned} S(x,y) =& \left(\frac{\delta^2\Gamma}{\delta\overline{\psi}(x)\delta\psi(y)}|_{\psi=\overline{\psi}=A^\mu=0}\right)^{-1} \\ G^{\mu\nu}(x,y) =& \left(\frac{\delta^2\Gamma}{\delta A^\mu(x)\delta A^\nu(y)}|_{\psi=\overline{\psi}=A^\mu=0}\right)^{-1}. \end{aligned} \tag{B.11}$$

We start with the photon propagator. Performing a functional derivative on equation (B.10) with respect to $A^\mu(y)$ yields

$$\begin{aligned} (G^{-1})^{\mu\nu}(x,y) =& \left[\partial_\rho\partial^\rho g^{\mu\nu} - \left(1-\frac{1}{\xi}\right)\partial^\mu\partial^\nu\right]\delta^4(x-y) + \Pi^{\mu\nu}(x,y) \\ \Pi_{\mu\nu}(x,y) =& ie^2\int d^4z_1 d^4z_2 tr\left[\gamma_\mu S(x,z_1)\Gamma_\nu(y,z_1,z_2)S(z_2,x)\right] \end{aligned} \tag{B.12}$$

where

$$\Gamma_\nu(x,y,z) = \frac{\delta^3\Gamma}{e\delta A^\nu(x)\delta\overline{\psi}(y)\delta\psi(z)}|_{A_\nu=\psi=\overline{\psi}=0} \tag{B.13}$$

is the fermion-gauge-boson vertex[1]. To get an expression for the propagator in momentum space, we perform a Fourier transform on the first line in equation (B.12). The Ward Takahashi identity for the photon polarization tensor is $q_\mu \Pi^{\mu\nu}(q) = 0$, and therefore the polarization tensor has the form

$$\Pi^{\mu\nu}(q) = \left(-g^{\mu\nu}q^2 + q^\mu q^\nu\right)\Pi(q^2) \tag{B.14}$$

where $\Pi(q)$ is a scalar function. Performing the inversion yields

$$G^{\mu\nu}(q) = \frac{-g^{\mu\nu} + \left(\frac{q^\mu q^\nu}{q^2+i\epsilon}\right)}{(q^2+i\epsilon)\left(1+\Pi(q^2)\right)} - \xi\frac{q^\mu q^\nu}{(q^2+i\epsilon)^2}. \tag{B.15}$$

The fermion propagator is obtained in the same way. Taking a functional derivative of Z with respect to $\overline{\psi}$ gives

$$\begin{aligned} 0 &= \int d\mu \frac{\delta}{\delta\overline{\psi}(x)} \exp\left(iS[\overline{\psi},\psi,A] + i\int d^4x\left[\left(\bar{\psi}\eta + \bar{\eta}\psi\right) + A_\mu J^\mu\right]\right) \\ &= \int d\mu \left(\frac{\delta S[\overline{\psi},\psi,A]}{\delta\overline{\psi}(x)} + \eta(x)\right)\exp\left(iS + i\int d^4x\left[\left(\bar{\psi}\eta + \bar{\eta}\psi\right) + A_\mu J^\mu\right]\right) \\ &= \left(\frac{\delta S[\overline{\psi},\psi,A]}{\delta\overline{\psi}(x)}\left[\frac{\delta}{i\delta J}, \frac{\delta}{i\delta\overline{\eta}}, -\frac{\delta}{\delta\eta}\right] + \eta(x)\right) Z. \end{aligned} \tag{B.16}$$

We can define a correction to the fermion propagator in the same way we did for the photon propagator. We call it the fermion self energy, or Σ. Following the same steps as above, we obtain

$$\begin{aligned} &\delta^4(x-y) = \left(i\not{\partial} - m\right)S(x,y) - ie^2\int d^4z_1 d^4z_2 d^4z_3\left(\gamma_\mu G^{\mu\nu}(x,z_1)S(x,z_2)\Gamma_\nu(z_1,z_2,z_3)S(z_3,y)\right) \\ &-i\Sigma(x,y) = e^2\int d^4z_1 d^4z_2 \gamma_\mu G^{\mu\nu}(x,z_1)S(x,z_2)\Gamma_\nu(z_1,z_2,y) \\ &\left(i\not{\partial} - m\right)S(x,y) - \int d^4z_1\Sigma(x,z_1)S(z_1,y) = \delta^4(x-y). \end{aligned} \tag{B.17}$$

Equations (B.12) and (B.17) for the photon and fermion self energy depend on the same vertex function, Γ_μ. This vertex should be obtained from its own SD equation (which

[1] to help with clarity, we would like to draw attention the difference between the generating functional Γ and the vertex function Γ_ν

will in turn depend on higher vertex functions), but at some point this infinite hierarchy must be truncated. Often the truncation is performed by inserting a bare vertex at some order. We will the ansatz described in section 2.2.

Appendix C

Parallelization

First some terminology. A node is an element of a computing system with its own shared memory across multiple cpu cores. It can be thought of as the larger grouping, or a superset of cores. Each core has its own logical units, memory handling, and may have multiple threads itself. For our purposes, it is sufficient to know that a core does a calculation, and a node is a collection of cores which all have access to the same memory system.

When the loops in a calculation's program have parts which are capable of being considered independently (not necessarily always, but at least for certain portions/steps of the calculation), it is possible to speed up the calculation by employing multiple cores to handle these independent sections simultaneously. It is usually most efficient to parallelize the outer-most loops of the program. In our calculation, this means parallelizing the loops for the momentum variables of the external legs of the fermion dressing functions. We started by using openMP (Open Multi-Processing) as the library for implementing this parallelization, and later found it beneficial to switch to MPI (Message Passing Interface). These two libraries are described in the next two sections.

C.1 Open MP

OpenMP's most outstanding advantage is that it is easy to use. To parallelize a loop, all that is required is a statement before and after the loop specifying it is to be parallelized, a call to get how many cores are available to be utilized, and a list specifying which variables are public and which are private across the cores. A public variable means it is the same for all proccesses, and a private one means it will vary across different cores. So for example, if we were to parallelize the p_0 loop of the outer leg, something like the coupling constant would be a public variable, whereas the value of the outer leg p_0 (or any function depending on it) would be private. There are also many other convenient variable definitions provided by the library, such as the reduction type, which considers the variable private during the calculation, but keeps track of the variables' value and combines them using an operator, such as addition, at the end of the parallelized region. This has obvious utility if you wish to parallelize the discretized integral (i.e. sum) across the inner legs.

OpenMP is based on the shared memory in a node. This is both an asset and a drawback depending on the nature of the calculation. It means there is less time wasted communicating information between different processors, but it means the number of cores available for use is limited by how many are in one node. This means a calculation will be better suited to openMP if it is high in RAM demand (the amount of data which must be made available to multiple cores) relative to the number of cores being used. In our calculation, this was not the case, which leads us to our next parallelization library.

C.2 MPI

MPI's advantage is that it is not restricted to the number of cores in a single node. It is capable of distributing specified information across many cores without shared memory like those in a single node. This can make things more complicated, especially if security

keys and permissions must be set up between the different elements communicating with each other. Like-wise, the actual writing of the code is more involved than with openMP. Instead of a preexisting subroutine dividing and distributing the loop elements among all available cores, it is left to the individual to write their own system for deciding which cores calculate which sections of the loop. When an MPI program is run, it starts identical programs (the number of which specified by the user at run time) which are each assigned their own id number. An if statement then differentiates whether the process is the "root" or a "child" and runs the appropriate code. The root is responsible for communicating the necessary information to each child, which then do their work, and send the information back to the root to be combined and prepared for the next iteration. All of the subroutines in the library deal with this communication, with Send() and Receive() being the most basic elements, doing exactly as you would expect with the information. There are also other subroutines which more succinctly handle sending the same information across multiple children, collecting information from children into one array, taking an array and distributing the parts equally among the children, etc.

MPI is advantageous for programs which have a large number of loop elements relative to the RAM requirements of the calculation. It can run many more cores at a time, but is slower at communicating information across different cores (as these cores cannot always take advantage of a shared memory system).

C.2.1 Distributing Tasks

The following is a section of the code which distributes portions of the integral to different processes.

```
1  diffloop:      do an_idpx=1,NNpx
2                 do an_idp =1,NNp
3                 do an_idp0=1,NNpo
4
5                  diff=abs((NNpo/an_idp0)*(NNp/an_idp)*&
```

```
6                   (NNpx/an_idpx)-num_procs)
7                   if(diff.eq.0) then
8                           p0avgrowsperproc=an_idp0
9                           pavgrowsperproc =an_idp
10                          pxavgrowsperproc=an_idpx
11                          exit diffloop
12                  end if
13
14                  end do
15                  end do
16                  end do diffloop
17
18                          p0procs=NNpo/p0avgrowsperproc
19                          pprocs =NNp/pavgrowsperproc
20                          pxprocs=NNpx/pxavgrowsperproc
21
22          p0id=0
23          pid =0
24          pxid=0
25
26          do an_id=0,num_procs-1
27
28                  p0startrow=p0id*p0avgrowsperproc+1
29                  p0endrow=p0startrow+p0avgrowsperproc-1
30
31                  pstartrow=pid*pavgrowsperproc+1
32                  pendrow=pstartrow+pavgrowsperproc-1
33
34                  pxstartrow=pxid*pxavgrowsperproc+1
```

```
35                pxendrow=pxstartrow+pxavgrowsperproc-1
36
37                if(pxid.ge.(pxprocs-1)) pxendrow = NNpx
38                if(pid.ge.(pprocs-1))   pendrow  = NNp
39                if(p0id.ge.(p0procs-1)) p0endrow = NNpo
40
41                pxid=pxid+1
42
43                if(pxid.eq.pxprocs) then
44                        pxid = 0
45                        pid  = pid+1
46                        if(pid.eq.pprocs)then
47                                pid  = 0
48                                p0id = p0id+1
49                        end if
50                end if
51
52                p0rowstosend=p0endrow-p0startrow+1
53                prowstosend=pendrow-pstartrow+1
54                pxrowstosend=pxendrow-pxstartrow+1
55
56                p0num_start_row_array(an_id)   =p0startrow
57                pnum_start_row_array (an_id)   =pstartrow
58                pxnum_start_row_array(an_id)   =pxstartrow
59                p0num_rows_to_send_array(an_id)=p0rowstosend
60                pnum_rows_to_send_array(an_id) =prowstosend
61                pxnum_rows_to_send_array(an_id)=pxrowstosend
62
63        end do
```

C.2.2 Reshaping Arrays

Due to technical issues, MPI is incapable of communicating multi-dimensional arrays in Fortran, and is only capable of handling 1-D arrays. To work around this, it was necessary to devise a way to move multi-dimensional arrays to 1-D arrays in a one-to-one manner.

```
1  do p0 = p0start_row, p0end_row
2  do p = pstart_row, pend_row
3  do pang = 1,pxArray % N1
4
5  !!!!!!!!!!!!!!!!!!!!!!!!!!!!!!!!!!!!!!!!!!!!!!!!!!!
6  !calculation of integral here
7  !!!!!!!!!!!!!!!!!!!!!!!!!!!!!!!!!!!!!!!!!!!!!!!!!!!
8
9
10         tempindex = 1 + (pang-1)*(p0num_rows_received*&
11         pnum_rows_received) +(p-pstart_row)*&
12         (p0num_rows_received) + p0 - p0start_row
13         tempZPArray1 % Array(tempindex)=ZpArray1 % yarray&
14         % array(p0,p,pang)
15         tempA1PArray1 % Array(tempindex)=ApArray1(1) %&
16         yarray % array(p0,p,pang)
17         tempA2PArray1 % Array(tempindex)=ApArray1(2) %&
18         yarray % array(p0,p,pang)
19         tempDPArray1 % Array(tempindex)=DpArray1 % yarray&
20         % array(p0,p,pang)
21         tempPiArray1 % Array(tempindex)=PiArray1 % yarray&
22         % array(p0,p,pang)
23
24 end do
```

```
25 end do
26 end do
27
28 !!!!!!!!!!!!!!!!!!!!!!!!!!!!!!!!!!!!!!!!!!!!!!!!!!!!
29 !communicating code goes here
30 !take all the temp<function>Array1 arrays and combine them
31 !into fulltemp<function>Array1 fulltemp<function>Array1
32 !is ordered by the id number of the processor
33 !!!!!!!!!!!!!!!!!!!!!!!!!!!!!!!!!!!!!!!!!!!!!!!!!!!!
34
35 do an_id = 0,num_procs-1
36
37         p0start_rowt = p0num_start_row_array(an_id)
38         p0num_rows_receivedt = p0num_rows_to_send_array(an_id)
39         p0end_rowt = p0start_rowt + p0num_rows_receivedt - 1
40         pstart_rowt = pnum_start_row_array(an_id)
41         pnum_rows_receivedt = pnum_rows_to_send_array(an_id)
42         pend_rowt =  pstart_rowt + pnum_rows_receivedt - 1
43
44         do p0 = p0start_rowt, p0end_rowt
45         do p = pstart_rowt, pend_rowt
46         do pang = 1,pxArray % N1
47
48         !this is the same as previous tempindex but shifted
49         !appropriately for the process id number
50
51         tempindex = 1 + (pang - 1)*(p0num_rows_received*&
52         pnum_rows_received) + (p - pstart_row)*&
53         (p0num_rows_received) + p0 - p0start_row + &
```

```
54          an_id*NNpx*p0num_rows_received*pnum_rows_received
55
56          ZpArray1 % yarray % array(p0,p,pang)=fulltempZPArray1 &
57          % Array(tempindex)
58          ApArray1(1) % yarray % array(p0,p,pang)=fulltempA1PArray1&
59          % Array(tempindex)
60          ApArray1(2) % yarray % array(p0,p,pang)=fulltempA2PArray1 &
61          % Array(tempindex)
62          DpArray1 % yarray % array(p0,p,pang)=fulltempDPArray1 &
63          % Array(tempindex)
64          PiArray1 % yarray % array(p0,p,pang)=fulltempPiArray1 &
65          % Array(tempindex)
66
67          end do
68          end do
69          end do
70
71  end do
```

Bibliography

[1] M. E. Carrington, C. S. Fischer, L. von Smekal, and M. H. Thoma. Dynamical gap generation in graphene with frequency dependent renormalization effects. *Physical Review B*, 94:125102–125111, 2016.

[2] M. E. Carrington, C. S. Fischer, L. von Smekal, and M. H. Thoma. The role of frequency dependence in dynamical gap generation in graphene. *Physical Review B*, 97:115411–115417, 2017.

[3] C. S. Fischer, R. Alkofer, T. Dahm, and P. Maris. Dynamical chiral symmetry breaking in unquenched QED_3. *Physical Review D*, 70:073007, 2004.

[4] E. V. Gorbar, V. P. Gusynin, and V. A. Miransky. Dynamical chiral symmetry breaking on a brane in reduced qed. *Physical Review D*, 64:105028–105044, 2001.

[5] V. P. Gusynin, S. G. Sharapov, and J. P. Carbotte. Ac conductivity of graphene: from tight-binding model to 2+1-dimensional quantum electrodynamics. *International Journal of Modern Physics B*, 21:4611–4658, 2007.

[6] A. Kizilersu, M. Reenders, and M. R. Pennington. One loop qed vertex in any covariant gauge: its complete analytic form. *Physics Review D*, 52:1242–1259, 1995.

[7] Valeri N. Kotov, Bruno Uchoa, Vitor M. Pereira, F. Guinea, and A. H. Castro Neto. Electron-electron interactions in graphene: Current status and perspectives. *Review of Modern Physics*, 84:1067–1129, 2010.

[8] Li, Zongping Chen, Wencai Ren, and Hui-Ming Cheng Feng Li. Flexible graphene-based lithium ion batteries with ultrafast charge and discharge rates. *PNAS*, 109:17360–17365, Oct 2012.

[9] Yu-Ming Lin, Alberto Valdes-Garcia, Shu-Jen Han, Damon B. Farmer, Inanc Meric, Yanning Sun, Yanqing Wu, Christos Dimitrakopoulos, Alfred Grill, Phaedon Avouris, and et al. Wafer-scale graphene integrated circuit. *Science*, 332:1294–1297, Jun 2011.

[10] E. C. Marino. Quantum electrodynamics of particles on a plane and the chern-simons theory. *Nuclear Physics B*, 408:551–564, 1993.

[11] A. H. Castro Neto, F. Guinea, N. M. R. Peres, K. S. Novoselov, and A. K. Geim. The electronic properties of graphene. *Review of Modern Physics*, 81:109–162, 2007.

[12] N. M. R. Peres. Colloquium: The transport properties of graphene: An introduction. *Review of Modern Physics*, 82:2673–2700, 2010.

[13] C. Popovici, C. S. Fischer, and L. von Smekal. Fermi velocity renormalization and dynamical gap generation in graphene. *Physical Review B*, 88:205429–205438, 2013.

[14] Dharmendar Reddy, Leonard F Register, Gary D Carpenter, and Sanjay K Banerjee. Graphene field-effect transistors. *Journal of Physics D: Applied Physics*, 45(1):019501, Sep 2011.

[15] Anand Sharma, Valeri N. Kotov, and Antonio H. Castro Neto. Excitonic mass gap in uniaxially strained graphene. *Phys. Rev. B*, 95:235124, Jun 2017.

[16] Hai-Xiao Xiao, Jing-Rong Wang, Hong-Tao Feng, Pei-Lin Yin, and Hong-Shi Zong. Dynamical gap generation in 2d dirac semimetal with deformed dirac cone. *Physics Review B*, 96:155114–155126, 2017.

[17] Yu Zhu, Zhengzong Sun, Zheng Yan, Zhong Jin, and James M. Tour. Rational design of hybrid graphene films for high-performance transparent electrodes. *ACS nano*, 5 8:6472–9, 2011.